

## Seasonal variation of the HDO/H<sub>2</sub>O ratio in the atmosphere of Mars at the middle of northern spring and beginning of northern summer



Shohei Aoki<sup>a,b,\*</sup>, Hiromu Nakagawa<sup>b</sup>, Hideo Sagawa<sup>c</sup>, Marco Giuranna<sup>a</sup>, Giuseppe Sindoni<sup>a</sup>, Alessandro Aronica<sup>a</sup>, Yasumasa Kasaba<sup>b</sup>

<sup>a</sup> Istituto di Astrofisica e Planetologia Spaziali (IAPS), Istituto Nazionale di Astrofisica (INAF), Via del Fosso del Cavaliere 100, 00133 Roma, Italy

<sup>b</sup> Department of Geophysics, Tohoku University, Sendai, Miyagi 980-8578, Japan

<sup>c</sup> Faculty of Science, Kyoto Sangyo University, Motoyama, Kamigamo, Kita-ku, Kyoto 603-8555, Japan

### ARTICLE INFO

#### Article history:

Received 10 August 2014

Revised 10 June 2015

Accepted 16 June 2015

Available online 21 June 2015

#### Keywords:

Infrared observations

Mars, atmosphere

Spectroscopy

### ABSTRACT

We present the seasonal variation of the HDO/H<sub>2</sub>O ratio caused by sublimation–condensation processes in a global view of the martian water cycle. The HDO/H<sub>2</sub>O ratio was retrieved from ground-based observations using high-dispersion echelle spectroscopy of the Infrared Camera and Spectrograph (IRCS) of the Subaru telescope. Coordinated joint observations were made by the Planetary Fourier Spectrometer (PFS) onboard Mars Express (MEX). The observations were performed during the middle of northern spring ( $L_s = 52^\circ$ ) and at the beginning of summer ( $L_s = 96^\circ$ ) in Mars Year 31. The retrieved latitudinal mean HDO/H<sub>2</sub>O ratios are  $4.1 \pm 1.4$  ( $L_s = 52^\circ$ ) and  $4.4 \pm 1.0$  ( $L_s = 96^\circ$ ) times larger than the terrestrial Vienna Standard Mean Ocean Water (VSMOW). The HDO/H<sub>2</sub>O ratio shows a large seasonal variation at high latitudes. The HDO/H<sub>2</sub>O ratio significantly increases from  $2.4 \pm 0.6$  wrt VSMOW at  $L_s = 52^\circ$  to  $5.5 \pm 1.1$  wrt VSMOW at  $L_s = 96^\circ$  over the latitude range between  $70^\circ\text{N}$  and  $80^\circ\text{N}$ . This can be explained by preferential condensation of HDO vapor during the northern fall, winter, and spring and sublimation of the seasonal polar cap in the northern summer. In addition, we investigated the geographical distribution of the HDO/H<sub>2</sub>O ratio over low latitudes at the northern spring in the longitudinal range between  $220^\circ\text{W}$  and  $360^\circ\text{W}$ , including different local times from 10 h to 17 h. We found the HDO/H<sub>2</sub>O ratio has no significant variation ( $5.1 \pm 1.2$  wrt VSMOW) over the entire range. Our observations suggest that the HDO/H<sub>2</sub>O distribution in the northern spring and summer seasons is mainly controlled by condensation-induced fractionation between the seasonal northern polar cap and the atmosphere.

© 2015 Elsevier Inc. All rights reserved.

### 1. Introduction

Since the first discovery of water vapor in the martian atmosphere using ground-based observations (Spinrad et al., 1963), the investigation of the water cycle on Mars has been one of the central topics of martian planetary science. Space-borne observations have revealed that the global and seasonal distribution of water vapor is mainly controlled by dynamics and sublimation–condensation process between the atmosphere and the polar caps. Sublimation of water ice from the northern polar cap during spring and summer provides water vapor to the whole planet, and the water vapor re-condenses to the polar cap in fall and winter (e.g., Farmer et al., 1977; Smith, 2002; Fedorova et al., 2006; Fouchet et al., 2007; Maltagliati et al., 2008; Smith et al., 2009a). In addition

to the polar latitudes, the observations have revealed the geographical distribution of water vapor at the low–middle latitudes. Two local maxima of the water vapor amount located over Tharsis ( $\sim 120^\circ\text{W}$ ) and Arabia Terra ( $\sim 330^\circ\text{W}$ ) were identified at middle latitudes. The maxima could be caused by atmospheric dynamics or possible release of water from the subsurface. In addition to the presence of water vapor, water ice clouds form when water vapor in the atmosphere is saturated. Thus far, two major distributions of water ice clouds have been identified (e.g., Montmessin et al., 2004). One is observed at particular low-latitude regions and is called as the “equatorial cloud belt (ECB).” This is where the air is cooled in the ascending branch of the Hadley cell during the northern spring–summer season (e.g., Smith, 2004). The other major distribution of water ice clouds occurs at middle–high latitudes and is referred to as the “polar hood clouds”. These appear during the fall and spring seasons (e.g., Benson et al., 2011). In addition to the ice clouds in the atmosphere, the Gamma Ray Spectrometer (GRS) onboard Mars Odyssey

\* Corresponding author at: Istituto di Astrofisica e Planetologia Spaziali (IAPS), Istituto Nazionale di Astrofisica (INAF), Via del Fosso del Cavaliere 100, 00133 Roma, Italy.

discovered signals associated with subsurface water ice in the upper  $\sim 1\text{--}2$  m of soil (e.g., Boyton et al., 2002; Feldman et al., 2004). Hydrogen-rich deposits (between 20% and 100% water-equivalent by mass) were found at high latitudes ( $>50^\circ$ ). It suggests that there are large underground water reservoirs at high latitudes. In fact, Phoenix uncovered a shallow ice table at the landing site ( $68.22^\circ\text{N}$ ) (Smith et al., 2009b). Moreover, the hydrogen-rich deposits were found not only at high latitudes, but also in low-latitude regions. The water content in low-latitude regions never drops below  $\sim 2\%$  water-equivalent hydrogen by mass and can be as high as 8–10% around  $330^\circ\text{W}$  and  $175^\circ\text{W}$ . It implies that the subsurface water ice may present at low-latitude regions.

Water on Mars exists as vapor in the atmosphere, ice in the form of ice clouds, surface ice, and subsurface ice. The phase change between vapor and ice occurs via a sublimation–condensation process. Spatial and temporal variation of water vapor on Mars should be inseparably connected with this sublimation–condensation process. However, from the currently available observations of atmospheric  $\text{H}_2\text{O}$  on Mars, we cannot discriminate between several different physical mechanisms, e.g., atmospheric dynamics circulation, sublimation from and condensation to polar cap ice or ice clouds, and exchange with the subsurface reservoir. Mapping of the  $\text{HDO}/\text{H}_2\text{O}$  ratio allows us to infer the sublimation–condensation process. In the terrestrial case, global mapping of the  $\text{HDO}/\text{H}_2\text{O}$  ratio from a space satellite identified regions of strong evapotranspiration and condensation of water vapor (e.g., Frankenberg et al., 2009). Similar mapping of isotopic fractionation in water vapor is expected to provide deeper insight into the physical processes of the water cycle on Mars. The key theory is that the condensation process induces isotopic fractionation of water vapor due to the difference in vapor pressure. Heavier  $\text{HDO}$  vapor preferentially condensates compared to lighter  $\text{H}_2\text{O}$  vapor (e.g., Fouchet and Lellouch, 2000). Montmessin et al. (2005) calculated seasonal variations of the  $\text{HDO}/\text{H}_2\text{O}$  ratio using the General Circulation Model (GCM). They predicted that the  $\text{HDO}/\text{H}_2\text{O}$  ratio changes by a factor of 2 owing to condensation-induced fractionation in the polar region. On the other hand, no isotopic fractionation has been expected during sublimation owing to very slow molecular rate of diffusion within ice. However, a recent experimental study reported that the  $\text{HDO}/\text{H}_2\text{O}$  ratio of the sublimated gas is decreased from the bulk ratio when mineral dust present in the water ice such as the martian polar caps (Moores et al., 2012). Thus, it is still an open question whether isotopic fractionation occurs or not during sublimation of the polar caps on Mars.

$\text{HDO}/\text{H}_2\text{O}$  ratio also has been used as a proxy to understand of the atmospheric evolution of Mars. Previous observations showed that the mean  $\text{HDO}/\text{H}_2\text{O}$  ratio in the current martian atmosphere is 5–6 times larger than the terrestrial standard (Vienna Standard Mean Ocean Water, VSMOW;  $\text{HDO}/\text{H}_2\text{O} = 3.11 \times 10^{-4}$ ). This is probably due to atmospheric evolution, i.e., preferential escape of H atoms from the atmosphere into space for an extended period of time (e.g., Owen et al., 1988; Krasnopolsky et al., 1997; Webster et al., 2013). Understanding of the current water isotope variations in time and space can help to reveal the water history of Mars, because such variations can constrain the distribution of water reservoirs on Mars (e.g., Fisher, 2007).

So far, the distribution of the  $\text{HDO}/\text{H}_2\text{O}$  ratio has been investigated using only a few ground-based observations (e.g., Fisher et al., 2008; Novak et al., 2011). Fisher et al. (2008) showed that the  $\text{HDO}/\text{H}_2\text{O}$  ratio was not uniform but it varied within a range between 2 and 10 wrt VSMOW depending on latitude and season using the data by Mumma et al. (2003). Novak et al. (2011) found latitudinal gradients of the  $\text{HDO}/\text{H}_2\text{O}$  ratio at  $L_s = 50^\circ$  (northern middle spring). Relatively low ratios at high latitudes were interpreted as the effect of condensation of  $\text{HDO}$  vapor over high

latitudes at the middle of the northern spring. Recently, Villanueva et al. (2015) reported global maps of  $\text{HDO}/\text{H}_2\text{O}$  ratio at  $L_s = 335^\circ$  (northern late winter),  $L_s = 50^\circ$  (northern middle spring), and  $L_s = 80^\circ$  and  $83^\circ$  (northern late spring). They claimed that the averaged  $\text{HDO}/\text{H}_2\text{O}$  ratio is  $\sim 7$  wrt VSMOW, which is larger than the previous observations by Owen et al. (1988) and Krasnopolsky et al. (1997). Moreover, they found correlation among  $\text{HDO}/\text{H}_2\text{O}$  ratio, atmospheric temperature, and  $\text{H}_2\text{O}$  column abundance, and possible anti-correlation between  $\text{HDO}/\text{H}_2\text{O}$  ratio and surface altitude. In addition, they found very low  $\text{HDO}/\text{H}_2\text{O}$  ratio (1–3 wrt VSMOW) at the winter hemisphere. Isotopic fractionation induced by sublimation–condensation process could explain some of the latitudinal variability, however, the phase change fractionation could not explain the reported non-uniform distribution. It might imply existence of multiple ice reservoirs having different  $\text{HDO}/\text{H}_2\text{O}$  ratios depending on their size, accessibility, and location (Fisher, 2007).

To improve our observational knowledge of this topic, we investigated the  $\text{HDO}/\text{H}_2\text{O}$  ratio during two different seasons, the northern spring ( $L_s = 52^\circ$ ) and summer ( $L_s = 96^\circ$ ), to reveal the seasonal variation. The comparison of two different seasons is expected to assist in the identification of the physical processes that cause the non-uniform distribution of  $\text{HDO}/\text{H}_2\text{O}$ . We performed ground-based observations using high-dispersion echelle spectroscopy ( $\lambda/\Delta\lambda \sim 20,000$ ) of the Infrared Camera and Spectrograph (IRCS) of the Subaru telescope (8.2 m) at the Mauna Kea observatory and coordinated joint observations with the Planetary Fourier Spectrometer (PFS) onboard the Mars Express (MEX).

## 2. Observations

### 2.1. Ground-based observations with Subaru/IRCS

Our ground-based observations by Subaru/IRCS were performed on January 4–5, 2012 and April 13, 2012. Table 1 summarizes the observation conditions. The observed seasons on Mars correspond to spring ( $L_s = 52.4^\circ$  and  $L_s = 52.9^\circ$ ) and summer ( $L_s = 96.2^\circ$ ) in the northern hemisphere of Mars for January 2012 and April 2012, respectively. The observational diameters of Mars were 9.3–9.4 and 11.5 arcsec on January 4–5 and on April 13, respectively. Doppler shift between Mars and Earth was  $-15$  km/s on January 4–5 and  $+11$  km/s on April 13. During these observations, the longitude of the sub-Earth point varied from  $256^\circ\text{W}$  to  $302^\circ\text{W}$  at  $23.6^\circ\text{N}$  on January 4, from  $237^\circ\text{W}$  to  $294^\circ\text{W}$  at  $23.6^\circ\text{N}$  on January 5, and from  $34^\circ\text{W}$  to  $60^\circ\text{W}$  at  $22.3^\circ\text{N}$  on April 13. The longitude of the sub-solar point varied from  $292^\circ\text{W}$  to  $339^\circ\text{W}$  at  $19.7^\circ\text{N}$  on January 4, from  $273^\circ\text{W}$  to  $330^\circ\text{W}$  at  $19.8^\circ\text{N}$  on January 5, and from  $344^\circ\text{W}$  to  $19^\circ\text{W}$  at  $25.0^\circ\text{N}$  on April 13, 2012.

IRCS is designed to deliver diffraction-limited images at  $2\text{--}5$   $\mu\text{m}$ , as well as to provide spectroscopy with grisms and a cross-dispersed echelle (Kobayashi et al., 2000). We used the high-dispersion echelle mode in L-band ( $2.85\text{--}4.16$   $\mu\text{m}$ ) and the camera with a J-band filter ( $1.25 \pm 0.16$   $\mu\text{m}$ ) as a slit viewer. IRCS has a  $1024 \times 1024$  pixel InSb array detector with a pixel size of  $0.055$  arcsec (slit length direction)  $\times$   $0.068$  arcsec (slit width direction). The longest and narrowest slit ( $6.69$  arcsec  $\times$   $0.14$  arcsec) was used to maximize the spatial coverage and spectral resolving power that features an instrumental resolving power of  $\sim 20,000$  with a sampling rate of  $\sim 40,000$ . The high spectral resolution of IRCS is essential for this study because the lines of martian  $\text{HDO}$  and  $\text{H}_2\text{O}$  are quite narrow (line width  $\sim 0.005$   $\text{cm}^{-1}$ ).

The slit was placed along the north–south direction to investigate latitudinal distribution covering the northern pole during the observations on January 5 and April 13. The slit was fixed at the sub-Earth longitude that advances at a rate of about

**Table 1**  
Parameters of Mars observations with Subaru/IRCS.

Date and time (UT)	Ls (°)	MY	Doppler shift (km/s)	Diameter (")	Airmass	Slit direction	Observing areas (°)	Local time
4/January/2012 13:12–16:26	52.4	31	–15	9.3	1.14–1.09	E–W	0N–40N	10–17
5/January/2012 12:34–16:28	52.9	31	–15	9.4	1.25–1.10	N–S	256W–302W	13–15
13/April/2012 8:24–10:49	96.2	31	+11	11.5	1.05–1.56	N–S	34W–60W	9–10

15° in martian longitude per hour local time (due to planetary rotation of Mars). During the observation on January 4, however, the slit was oriented along the east–west direction to investigate longitudinal distribution. For this latter case, we obtained the spectra at 15 latitudes from 0°N to 40°N by manually setting the slit on different positions.

We nodded the telescope along the slit observing Mars and sky in the A and B positions, respectively, with a difference of 30 arcsec. Subtraction of (A–B) removes the telluric emissions and other instrumental features. Flat field was obtained immediately before and after the observations. In addition, we performed standard star (*Denebola* on January 4–5 and *Regulus* on April 13) measurements at the beginning, middle, and end of each observation and Ar lamp measurements in order to investigate the instrumental line shape of IRCS.

An example of the spectrum measured by IRCS is shown in Fig. 1. Owing to the cross-dispersion, we could measure the following five spectral bands simultaneously: 2.94–3.01  $\mu\text{m}$  (Order-19 of the IRCS grating), 3.01–3.18  $\mu\text{m}$  (Order-18), 3.28–3.36  $\mu\text{m}$  (Order-17), 3.49–3.57  $\mu\text{m}$  (Order-16), and 3.72–3.81  $\mu\text{m}$  (Order-15). The observed spectra exhibit strong absorption lines of CO<sub>2</sub> (627), CO<sub>2</sub> (628), and HDO at Order-15, CO<sub>2</sub> (626) at Order-16, CH<sub>4</sub> at Order-16 and 17, and H<sub>2</sub>O at Order-17, 18, and 19. The wide spectral coverage of IRCS allows us to observe H<sub>2</sub>O and HDO features simultaneously. The spatial resolution of our measurements is mainly restricted by the atmospheric seeing on the observation dates,  $\sim 0.8$  arcsec on January 4–5 and  $\sim 0.5$  arcsec on April 13. For the H<sub>2</sub>O and HDO analysis, the measured spectra were binned over 10 pixels ( $\sim 0.55$  arcsec) along the slit to increase signal to noise ratio.

## 2.2. Coordinated joint observation by MEX/PFS

PFS is a double-pendulum interferometer mainly designed for atmospheric analyses, such as measuring the 3-D temperature field in the lower atmosphere, the variations of minor constituents, and the optical properties of aerosols (Formisano et al., 2005). It has two spectral channels, one is the Short Wavelength Channel (SWC) and the other is the Long Wavelength Channel (LWC). The SWC covers the spectral range between 1750 and 8200  $\text{cm}^{-1}$  and the LWC covers the spectral range between 250 and 1700  $\text{cm}^{-1}$ , both with a sampling step of 1.0  $\text{cm}^{-1}$ . The spectral resolution is 1.3  $\text{cm}^{-1}$  without apodization and 2  $\text{cm}^{-1}$  when a Hamming function is applied to the interferograms. One of the advantages of PFS is its wide spectral coverage combined with relatively high spectral resolution.

We planned and performed coordinated joint measurements by MEX/PFS from April 10 to 16 (within  $\pm 3$  days from the Subaru/IRCS observation). The original purpose of this joint observation was to compare H<sub>2</sub>O retrievals between IRCS and PFS. However, the abundances of H<sub>2</sub>O could not be retrieved from the IRCS data because of the high terrestrial humidity during the joint observation. Therefore, the PFS measurements were used to retrieve H<sub>2</sub>O abundances and were subsequently coupled with the HDO data from Subaru/IRCS to derive the HDO/H<sub>2</sub>O ratio (there was no problem

retrieving both H<sub>2</sub>O and HDO from Subaru/IRCS data for the other observations carried out in January 2012). During the planned period (April 10–16) of the coordinated observations, PFS observations were performed in 26 orbits across Mars (MEX orbit #10541–10567). Unfortunately, PFS had some problems with the motion of the double-pendulum during this period of simultaneous observation with the Subaru/IRCS. However, PFS worked nominally in the 4 orbits listed in Table 2 and these observations have been successfully included in this work (as quasi simultaneous observations).

## 3. Method of analysis

### 3.1. Retrieval of H<sub>2</sub>O and HDO abundances from Subaru/IRCS data

We retrieved H<sub>2</sub>O abundances from the absorption lines at 3035.78356  $\text{cm}^{-1}$  (3.29  $\mu\text{m}$ , Order-17) and 3216.52218  $\text{cm}^{-1}$  (3.10  $\mu\text{m}$ , Order-18) and HDO abundances from the lines at 2672.59294  $\text{cm}^{-1}$  and 2677.71967  $\text{cm}^{-1}$  (both around 3.74  $\mu\text{m}$ , Order-19). We performed retrievals for each line independently in order to evaluate the accuracy of our retrievals. Table 3 describes the line parameters obtained from the HITRAN 2008 database (Rothman et al., 2009). As shown in Fig. 1, there are multiple H<sub>2</sub>O and HDO lines in the measured spectral range. However, most of the H<sub>2</sub>O lines are saturated or not strong enough, and CO<sub>2</sub> isotopic lines under the finite spectral resolution of IRCS contaminate most of the HDO lines on the measured spectra. We carefully selected the absorption lines to be used in this work. The selected lines satisfy the following conditions: strong enough (i.e., line strength is order of  $10^{-22}$  for H<sub>2</sub>O and  $10^{-24}$  for HDO), not saturated, minimal instrumental effect (i.e., line center is stable within  $\sim 1$  pixel along the slit), and minimal contamination from the other lines (i.e., the other terrestrial [O<sub>3</sub>, N<sub>2</sub>O, CH<sub>4</sub>, and H<sub>2</sub>O isotopes], martian CO<sub>2</sub>, and solar lines).

Since the martian H<sub>2</sub>O and HDO lines appear on the wings of the deep terrestrial ones (the martian lines are shifted  $\sim 2$  pixels from the terrestrial lines due to the Doppler shift), the contribution from the terrestrial atmosphere should be separated in order to extract the martian lines. The extraction requires special considerations of the narrowness of the martian lines ( $\sim 1/10$  of the IRCS spectral resolution) and of the intrinsic (anamorphic) optical properties of IRCS that lead to an irregular mapping of the spatial and spectral dimensions on to the detector array. For removal of telluric absorptions, co-measured spectra of nearby reference stars are often used in ground-based observations. However, extrapolating the reference star (point-source) signal to an extended object introduces systematic errors. In addition, since the method with standard stars requires atmospheric stability and the same observed air mass between the target and reference stars, it does not always guarantee the quality of the calibration. To solve these problems, we numerically synthesized the terrestrial atmospheric opacity by developing a dedicated line-by-line radiative transfer model and fitted it to the measurement spectra to obtain the telluric absorptions during our observations.

Our model is based on clear-sky atmosphere model and takes into account the atmospheric opacities due to terrestrial lines of

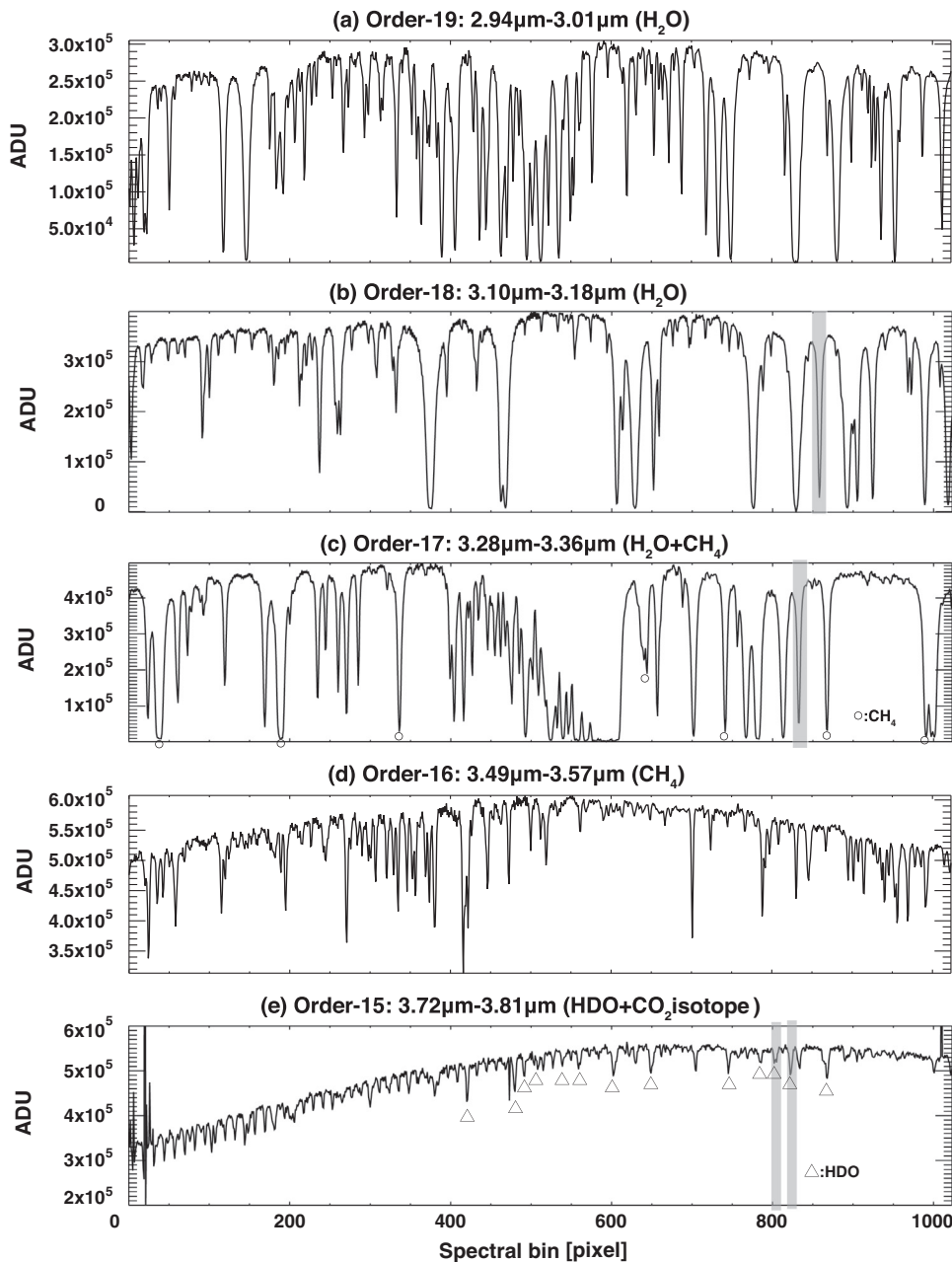


**Fig. 1.** Example of a spectrum obtained by IRCS. Five spectral bands can be observed simultaneously: 2.94–3.01  $\mu\text{m}$  (order-19), 3.01–3.18  $\mu\text{m}$  (order-18), 3.28–3.36  $\mu\text{m}$  (order-17), 3.49–3.57  $\mu\text{m}$  (order-16), and 3.72–3.81  $\mu\text{m}$  (order-15). The spectrum was observed on January 5 with 5-min integration and without binning. Circular symbols in (c) represent  $\text{CH}_4$  lines and the other features in Order-17 are  $\text{H}_2\text{O}$  lines. Triangle symbols in (e) represent the HDO lines. The gray boxes represent the spectral ranges used in this analysis.

**Table 2**  
PFS orbits used for the joint observation with Subaru/IRCS.

Orbit number	Date (UT)	Longitude ( $^{\circ}\text{W}$ )	Local time (h)
#10542	10/April/2012 12:21–13:20	16	16
#10547	11/April/2012 23:08–24:06	167	16
#10554	13/April/2012 23:47–25:14	162	16
#10557	14/April/2012 20:45–22:12	109	16

$\text{H}_2\text{O}$ , HDO, and  $\text{O}_3$ , martian lines of  $\text{H}_2\text{O}$ , HDO, and  $\text{CO}_2$  isotopologues (626, 627, 638), solar lines, and the instrumental line shape of IRCS. The line parameters were obtained from the HITRAN 2008

spectroscopic database (Rothman et al., 2009). Isotopic ratios of  $\text{CO}_2$  (627) and  $\text{CO}_2$  (638) were obtained from recent results by Curiosity/TLS (Webster et al., 2013; reported isotopic ratios of  $\text{CO}_2$  (627) and  $\text{CO}_2$  (638) are  $7.618 \times 10^{-4}$  and  $4.928 \times 10^{-5}$ , respectively). The expected signal intensity  $I(x_0)$  at pixel-point  $x_0$  was calculated as follows:

$$I(x_0) = [(ax + b) \times t_{\text{solar}}(x) \times \exp(-\tau_E(x) - \tau_M(x))] \otimes ILS(x_0 - x, w_{ILS}),$$

where  $x$  is pixel-point with a sampling rate of ten milli-pixels ( $x_0$  and  $x$  are a function of wavelength),  $a$  and  $b$  are the scaling factors for continuum,  $t_{\text{solar}}$  is the transmittance of the solar lines,  $\tau_E$  is the total optical depth of the terrestrial lines,  $\tau_M$  is the total optical depth of the martian lines, and  $ILS$  is the instrumental line shape of IRCS. The transmittance of the solar spectrum was obtained from

**Table 3**Parameters of HDO and H<sub>2</sub>O lines used in this study. The values are taken from the HITRAN 2008 spectroscopic database (Rothman et al., 2009).

Molecular	H <sub>2</sub> O	H <sub>2</sub> O	HDO	HDO
Wavenumber (cm <sup>-1</sup> )	3035.78356	3216.52218	2672.59294	2677.71967
Intensity (cm) (for 296 K)	3.219 × 10 <sup>-22</sup>	2.848 × 10 <sup>-22</sup>	7.463 × 10 <sup>-24</sup>	9.117 × 10 <sup>-24</sup>
Lower state energy (cm <sup>-1</sup> )	446.6966	222.0528	116.4613	91.3302
Air-broadened half-width (cm <sup>-1</sup> atm <sup>-1</sup> ) (for modeling of terrestrial lines)	0.0702	0.1080	0.0969	0.0975
Temperature-dependence exponent for the half-width	0.32	0.76	0.77	0.77

the database of the high-spectral-resolution observation performed by the ACE/FTS (Hase et al., 2010). The instrumental line shape of IRCS was retrieved from Ar lamp measurements. Since this analysis is sensitive to the line shape and especially to its wing, accurate characterization of the ILS is indispensable to retrieve the martian H<sub>2</sub>O and HDO abundances correctly. We found that the instrumental line shape can be expressed as a function of one parameter (its width  $W_{ILS}$ ) depending on pixel position over the detector, and this function can be defined by a combination of two Gaussian functions (see Appendix A in detail). For calculations of the terrestrial lines, we considered 32 atmospheric layers from 4 km to 50 km. The vertical profiles of temperature, pressure, water vapor, and O<sub>3</sub> in the terrestrial atmosphere were obtained from US standard atmosphere. Since the line shapes of the terrestrial atmosphere are dominated by molecular collisions, we considered the collisional line width at each atmospheric layer and summed the optical depths along the 32 atmospheric layers:

$$\tau_E(x) = \sum_j \frac{\eta N_j S(T_j) \alpha_L(T_j, P_j) / dw}{\pi [(x - x_0)^2 + (\alpha_L(T_j, P_j) / dw)^2]} \times z_j,$$

where  $\tau_E(x)$  is the total optical depth at  $x$  pixel-point,  $\eta$  is the telluric air mass,  $N_j$  is the column abundance of the gas at the  $j$ th layer,  $T_j$  is the temperature at the  $i$ th atmospheric layer,  $S(T_j)$  is the line strength at  $T_j$  K,  $\alpha_L$  is the collisional line width,  $dw$  is the dispersion of the IRCS echelle mode in L-band (0.763 Å/pixel at order18, 0.809 Å/pixel at order-17, and 0.914 Å/pixel at order-15),  $x_0$  is the central pixel-point of the terrestrial line, and  $z_j$  is the thickness of the layer. The temperature correction of the line intensity is referred to Rothman et al. (1998) by using the total internal partition sum from Gamache et al. (2000).

Line width of H<sub>2</sub>O and HDO in the martian atmosphere is dominated by the Doppler line width (e.g., Krasnopolsky et al., 2004), because the pressure in the atmosphere is relatively low. Therefore, we computed the optical depth considering the Doppler line widths:

$$\tau_M(x) = \sum_j \frac{\mu N_j S(T_j)}{\sqrt{\pi} \alpha_D(T_j) / dw} \exp\left(-\left[\frac{(x - x_0 + ds/dw)}{\alpha_D(T_j) / dw}\right]^2\right) \times z_j,$$

where  $\tau_M(x)$  is the total optical depth at  $x$  pixel-point,  $\mu$  is the total air mass on Mars,  $\alpha_D$  is the Doppler line width, and  $ds$  is Doppler shift. For the martian atmosphere, we considered 10 atmospheric layers from 0 km to 20 km, and the vertical profiles of temperature, pressure, and water vapor were derived from Mars Climate Database ver-4.3 (<http://www-mars.lmd.jussieu.fr/mars/access.html>). We assumed the effects of dust and ice aerosols to be negligible at this wavelength; accordingly, these were not included in the radiative transfer calculation.

The measured signals include both solar radiation reflected at the martian surface (2-way path in the martian atmosphere: Sun–Mars–Earth) and the thermal radiation of the martian surface (1-way path: Mars–Earth). Thus, the total air mass  $\mu$  is given by

$$\mu = r_s(\mu_s + \mu_e) + (1 - r_s)\mu_e,$$

where  $r_s$  is the rate of solar radiation,  $(1 - r_s)$  represents the rate of the thermal radiation,  $\mu_s$  is the Sun-to-surface air mass, and  $\mu_e$  is the

surface-Earth air mass. Our radiative transfer model showed that the contribution of thermal radiation from the martian surface is negligible (i.e.,  $r_s = 1.0$ ) at the H<sub>2</sub>O spectral range. Conversely, at the HDO spectral range, the contribution of thermal radiation must be taken into account. The rate  $r_s$  was retrieved using a strong solar line at 2669.7849 cm<sup>-1</sup> by comparing the observed spectrum with the synthetic spectrum of the solar line. Fig. 2 shows the retrieved rate of surface radiation  $(1 - r_s)$  retrieved from the IRCS data. The rates are variable depending on surface albedo and temperature. The enhancement of surface radiation rate  $(1 - r_s)$  at 280–320°W and 0–20°N appeared in the January data can be explained by low surface albedo (Christensen et al., 2001), and the latitudinal gradient appeared in the April data can be explained by decrease of surface temperature toward polar region. The relatively high rate at high-latitude region (>70°N) found in January data is probably caused by high surface albedo due to the presence of the seasonal polar cap on the ground.

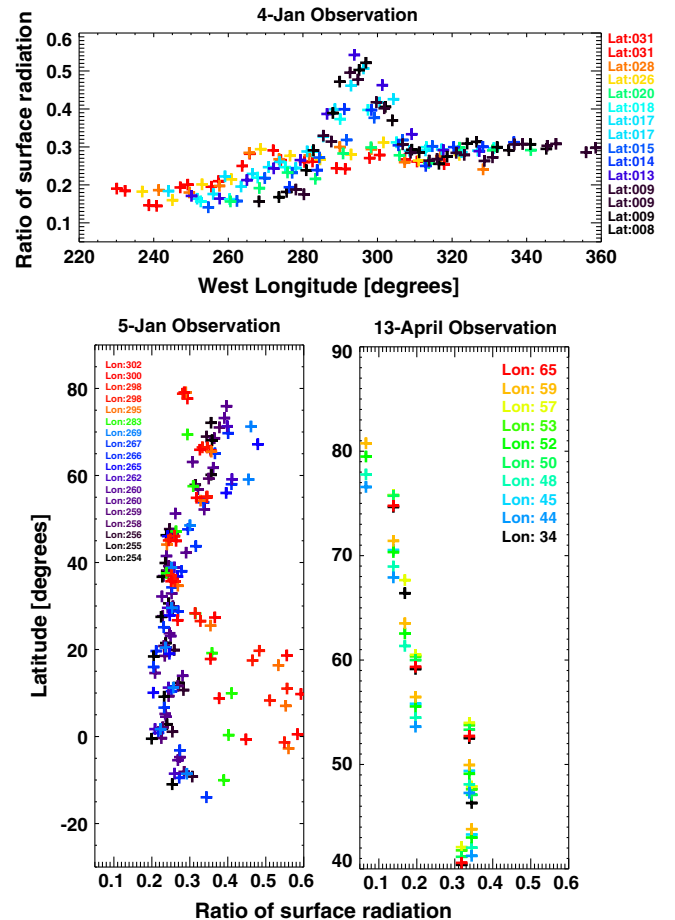


**Fig. 2.** Rate of surface radiation in the observed IRCS signals at HDO spectral range. Differences in colors show the observing latitudes or longitudes. (For interpretation of the references to color in this figure legend, the reader is referred to the web version of this article.)

For retrieval, the synthetic spectra were calculated in the limited spectral range of  $\pm 7$  pixels ( $\sim \pm 0.5 \text{ cm}^{-1}$ ) from the line center for each  $\text{H}_2\text{O}$  line, and  $\pm 5$  pixels ( $\sim \pm 0.3 \text{ cm}^{-1}$ ) from the line center for each HDO line. We retrieved the following five parameters: scaling factor for the continuum ( $a$  and  $b$ ), center pixel-point of the deep terrestrial line  $x_0$ , width of instrumental line shape  $w_{ILS}$ , total column density of the terrestrial water vapor, and total column density of the martian water vapor. We set the spectral resolution as an unknown parameter because it varies along the slit and dispersion direction. The total column density of the terrestrial water vapor was assumed as a constant value along the slit. The retrieval was performed by setting a parameter domain for the column density of martian water vapor from 0 pr- $\mu\text{m}$  to 25 pr- $\mu\text{m}$  with intervals of 1 pr- $\mu\text{m}$  for  $\text{H}_2\text{O}$  and 0 pr-nm to 100 pr-nm with intervals of 1 pr-nm for HDO. Then, for each condition of martian  $\text{H}_2\text{O}$  and HDO abundances, we retrieved the other 5 parameters using Levenberg–Marquardt non-linear minimization algorithm. Finally, we derived the martian  $\text{H}_2\text{O}$  and HDO column densities that provide the minimum values for chi-squares. To check our retrieval scheme, we applied the retrieval algorithm to standard star data as well as Mars observations. Figs. 3 and 4 show examples of the fitting analysis in the  $\text{H}_2\text{O}$  and HDO spectral ranges, respectively. No residual signal is present from the standard star observation, as expected. This indicates that the signal derived from Mars data represents the real martian contribution.

There are two sources of error in the retrieved martian  $\text{H}_2\text{O}$  and HDO abundances: instrumental noise and uncertainty in the forward (radiative transfer and IRCS instrumental) model. The instrumental noise was estimated from standard deviation (1-sigma) of the residuals between IRCS data and best-fit synthetic spectrum. Regarding the forward model error, the dominant factor is uncertainty in the temperature profile obtained from the Mars Climate Database, whose uncertainty is expected to be  $\sim 5\%$  (Sindoni et al., 2011). This uncertainty propagates to the errors in the retrieved  $\text{H}_2\text{O}$  abundances of  $\sim 7\%$  and  $\sim 1\%$  at  $3035 \text{ cm}^{-1}$  and  $3216 \text{ cm}^{-1}$ , and those in the retrieved HDO abundances of  $\sim 5\%$  and  $\sim 4\%$  at  $2672 \text{ cm}^{-1}$  and  $2677 \text{ cm}^{-1}$ , respectively. Finally, the uncertainties in the retrieved  $\text{H}_2\text{O}$  or HDO abundances  $\sigma$  were given by

$$\sigma = \sqrt{\sigma_n^2 + \sigma_m^2},$$

where  $\sigma_n$  is error due to instrumental noise, and  $\sigma_m$  represents error due to the model.

After the errors were evaluated, the  $\text{H}_2\text{O}$  abundances retrieved from the absorption lines at  $3035 \text{ cm}^{-1}$  and  $3216 \text{ cm}^{-1}$  and the HDO abundances from the lines at  $2672 \text{ cm}^{-1}$  and  $2677 \text{ cm}^{-1}$  were compared. We excluded results of the two retrieved values ( $\text{H}_2\text{O}$  or HDO abundances) that were inconsistent beyond  $2\sigma$  as “low confidence” results. Note that the inconsistent results were less than 15% of the whole data set. Lastly, the derived  $\text{H}_2\text{O}$  abundances, HDO abundances, and their errors were calculated from the weighted averages:

$$y = \frac{w_a y_a + w_b y_b}{w_a + w_b},$$

$$\sigma = \frac{1}{\sqrt{w_a + w_b}},$$

where  $y$  represents the derived  $\text{H}_2\text{O}$  or HDO abundance,  $y_a$  and  $y_b$  are the values retrieved from each of the lines, and  $w_a$  and  $w_b$  are given by

$$w_a = \frac{1}{\sigma_a^2},$$

$$w_b = \frac{1}{\sigma_b^2},$$

where  $\sigma_a$  and  $\sigma_b$  are the errors retrieved from each of the lines.

### 3.2. Retrieval of $\text{H}_2\text{O}$ abundances from MEX/PFS data

We retrieved  $\text{H}_2\text{O}$  abundances from PFS observations listed in Table 2. For the  $\text{H}_2\text{O}$  retrievals, the absorption band from  $3780$  to  $3950 \text{ cm}^{-1}$  at the Short Wavelength Channel (SWC) was used (Tschimmel et al., 2008; Sindoni et al., 2011). We averaged 9 consecutive spectra with a sampling rate of every two spectra in order to improve the SNR and the accuracy of the retrieved  $\text{H}_2\text{O}$  abundances. Fig. 5 shows an example of averaged PFS spectrum in the considered spectral range, and the best-fit synthetic spectrum. We retrieved  $\text{H}_2\text{O}$  abundances using a fast radiative transfer model developed for PFS data processing (Ignatiev et al., 2005) and least-squares method. The details of the retrieval algorithm can be found in Sindoni et al. (2011). The uncertainty in the retrieved  $\text{H}_2\text{O}$  mixing ratio is about 19% in total (Sindoni et al., 2011).

## 4. Latitudinal distribution at $L_s = 52^\circ$ (northern spring)

Fig. 6 shows latitudinal distribution of column-integrated  $\text{H}_2\text{O}$  and HDO abundances retrieved from Subaru/IRCS observations carried on January 5, 2012 ( $L_s = 52^\circ$ ) and the  $\text{H}_2\text{O}$  abundances taken from Mars Climate Database (MCD) ver-5.0 (<http://www-mars.lmd.jussieu.fr/mars/access.html>) for comparison. Different colors indicate the observed longitudes. These values have been normalized by surface pressure in order to remove the effect of topography. The retrieved  $\text{H}_2\text{O}$  abundances range from 4 pr- $\mu\text{m}$  to 15 pr- $\mu\text{m}$  (1 pr- $\mu\text{m} = 3.34 \times 10^{18} \text{ cm}^{-2}$ ), and exhibit maximum values around  $60\text{--}70^\circ\text{N}$ . On the other hand, the  $\text{H}_2\text{O}$  abundances predicted by MCD range from 5 pr- $\mu\text{m}$  to 15 pr- $\mu\text{m}$ , and show a maximum value around  $60^\circ\text{N}$ . Our observed  $\text{H}_2\text{O}$  abundances show general agreement with those from the MCD in terms of absolute values and latitudinal distribution. In addition, the longitudinal trend at the edge of Arabia Terra (over  $302^\circ\text{W}$  and  $298^\circ\text{W}$  at middle latitudes) appears both in the observation and model.

In the northern spring season ( $L_s = 52^\circ$ ), the edge of the northern polar cap is expected to be around  $70^\circ\text{N}$ , according to the observations by near-infrared spectroscopy (e.g., Appéré et al., 2011). Since surface temperature exceeds water condensation temperature at the edge of the polar cap, sublimation of the water ice cap would occur there. Indeed, the previous observations of water vapor during this season exhibit its enhancement at the edge of polar cap (e.g., Fouchet et al., 2007; Pankine et al., 2010). Thus, the enhancement of  $\text{H}_2\text{O}$  shown in our observations is likely due to sublimation of water ice.

The latitudinal distribution of HDO appears slightly different to that of  $\text{H}_2\text{O}$ . The retrieved HDO abundances range from 3 pr-nm to 17 pr-nm (1 pr-nm =  $3.34 \times 10^{15} \text{ cm}^{-2}$ ) and have a maximum value around  $30\text{--}40^\circ\text{N}$ . The difference between  $\text{H}_2\text{O}$  and HDO produces latitudinal gradients in the HDO/ $\text{H}_2\text{O}$  ratio. Fig. 7 shows the latitudinal distribution of the HDO/ $\text{H}_2\text{O}$  ratio retrieved from the Subaru/IRCS observation (left panel), their mean values averaged over the faced longitude ( $256\text{--}302^\circ\text{W}$ ), and values predicted by the GCM model of Montmessin et al. (2005) (right panel). The derived mean HDO/ $\text{H}_2\text{O}$  ratio ranges between  $5.0 \pm 0.9$  wrt VSMOW (at  $30^\circ\text{N}$ ) and  $2.4 \pm 0.6$  wrt VSMOW (at  $80^\circ\text{N}$ ). The global mean value of the HDO/ $\text{H}_2\text{O}$  ratio and its standard deviation are  $4.1 \pm 1.4$  wrt VSMOW. The distribution exhibits a maximum around sub-solar latitudes ( $20\text{--}40^\circ\text{N}$ ) and decreases at high latitudes ( $>60^\circ\text{N}$ ). As shown in Fig. 7, such a latitudinal gradient was also predicted by the GCM model based on condensation-induced fractionation (Montmessin et al., 2005). The model predicted that the HDO/ $\text{H}_2\text{O}$  ratio would decrease from 5 wrt VSMOW to 2 wrt VSMOW owing to preferential condensation of HDO vapor at high latitudes. We consider this depletion of HDO around  $50\text{--}80^\circ\text{N}$  is mainly due to the condensation of water vapor on the polar cap.

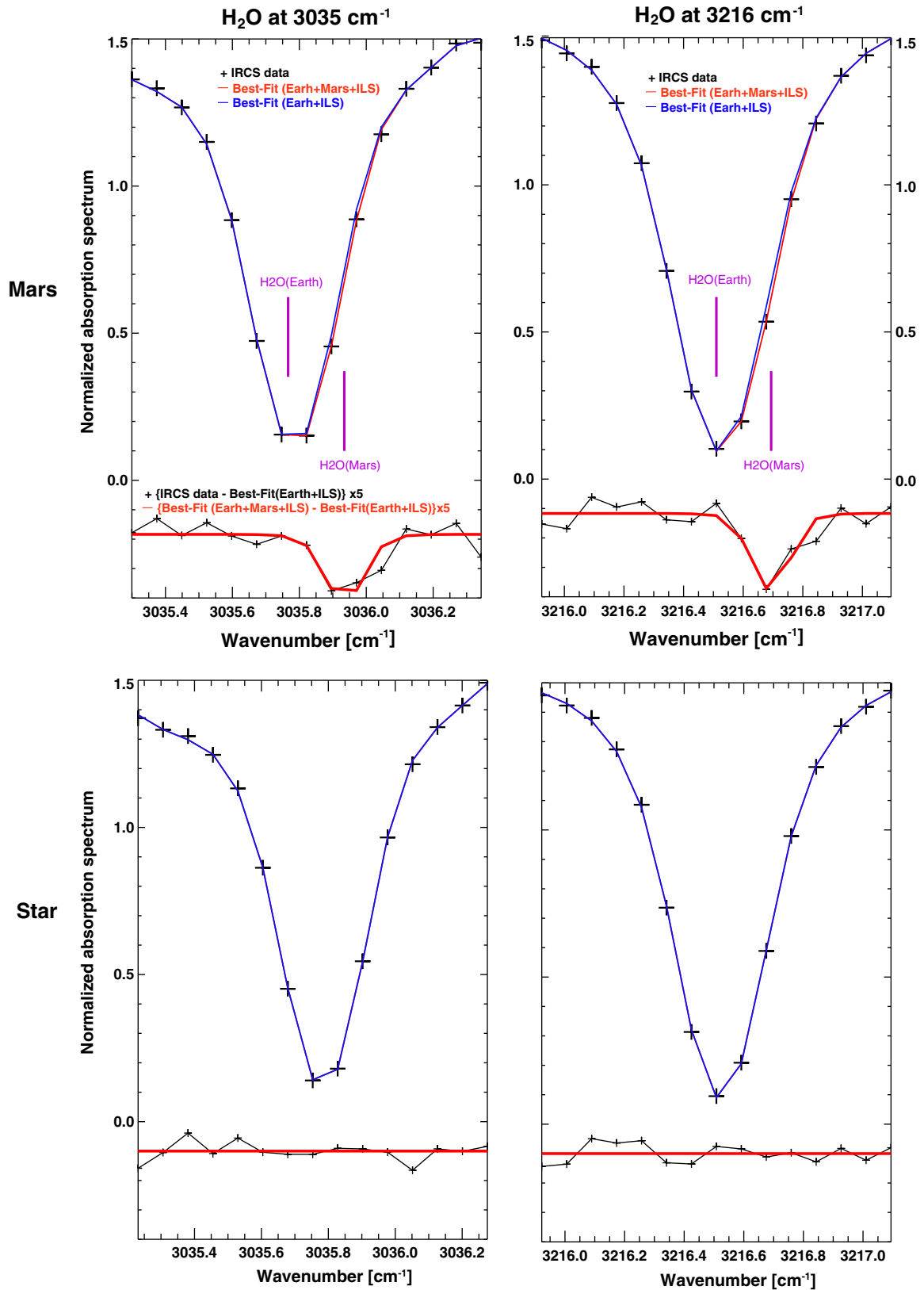


**Fig. 3.** Examples of the fitting analysis with Mars (top) and standard star (bottom) H<sub>2</sub>O lines. In the upper spectra at each panel, the IRCS data are shown in black and the best-fit synthetic spectra with and without martian contributions are in red and blue, respectively. The bottom spectra show residual spectra after removing the terrestrial contributions (Black: IRCS data, Red: the best-fit spectra). The martian spectra were measured on January 5, 2012 over the latitude 35°N. Retrieved column densities of martian H<sub>2</sub>O are 8 ( $\pm 2$ ) pr- $\mu\text{m}$  from 3035  $\text{cm}^{-1}$  ranges and 11 ( $\pm 1$ ) pr- $\mu\text{m}$  from 3216  $\text{cm}^{-1}$  ranges (1 pr- $\mu\text{m}$  equals  $3.34 \times 10^{18}$  molecules/ $\text{cm}^2$ ). (For interpretation of the references to color in this figure legend, the reader is referred to the web version of this article.)

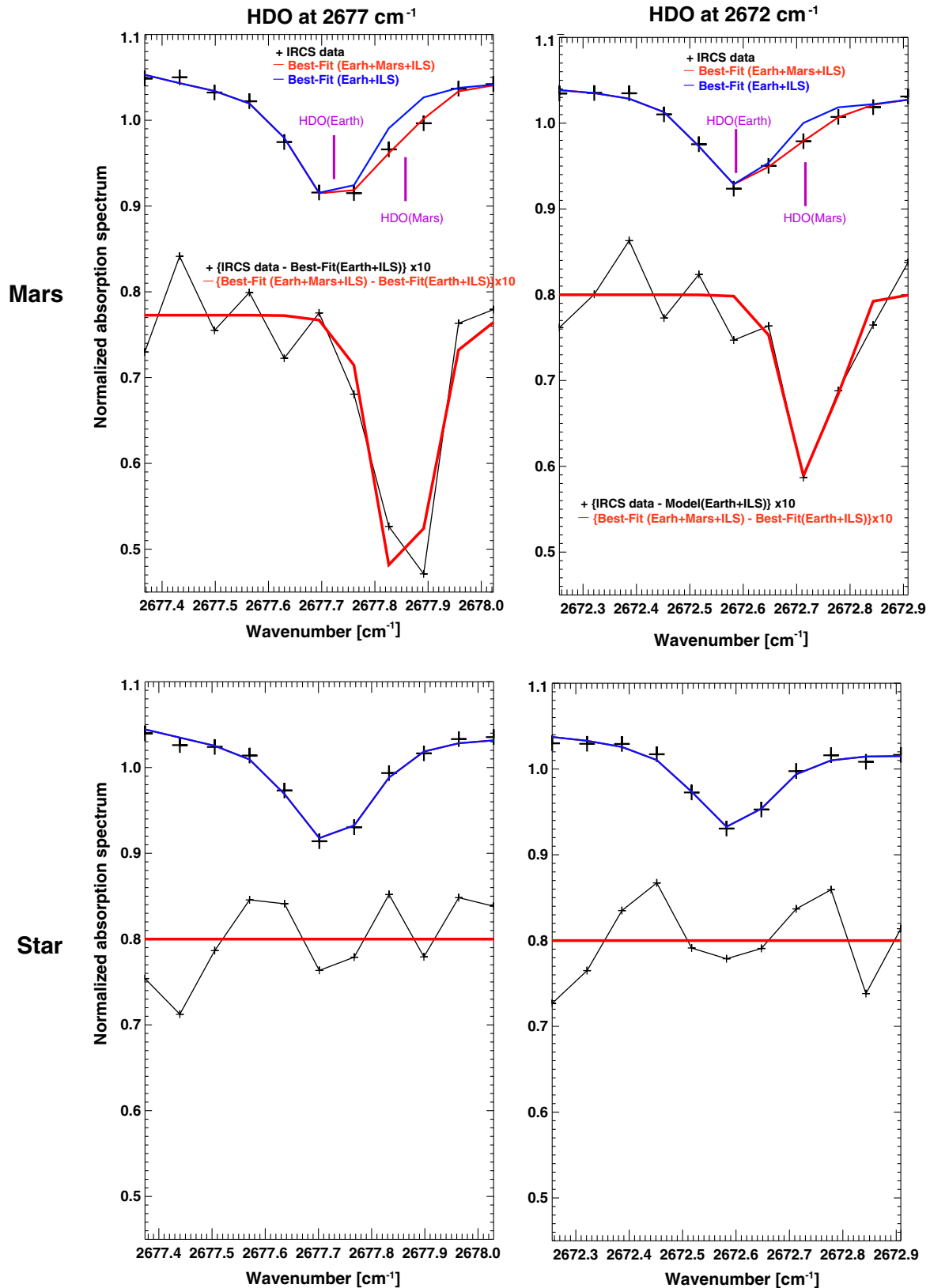
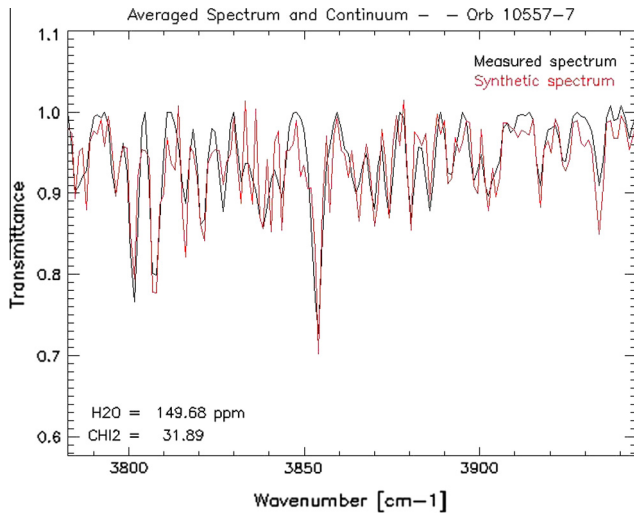


Fig. 4. Same as Fig. 3, but for HDO lines. Retrieved column densities of martian HDO are  $16 (\pm 4)$  pr-nm from  $2677 \text{ cm}^{-1}$  ranges and  $12 (\pm 3)$  pr-nm from  $2672 \text{ cm}^{-1}$  ranges.

In fact, the previous observation of surface composition detected the formation of a water ice cap over the polar cap at  $70\text{--}90^\circ\text{N}$  (e.g., Appéré et al., 2011) and the GCM suggested the formation of polar hood clouds at  $50\text{--}90^\circ\text{N}$  (Montmessin et al., 2004).

### 5. Latitudinal distribution at $L_s = 96^\circ$ (northern summer)

We retrieved the latitudinal distribution of the HDO/H<sub>2</sub>O ratio during the northern summer ( $L_s = 96^\circ$ ) using HDO abundance



**Fig. 5.** An example of retrieval of H<sub>2</sub>O abundance from PFS/SWC data at 13.3°N. The black curve shows the averaged PFS spectrum and the red one represents the best-fit synthetic spectrum. The retrieved H<sub>2</sub>O mixing ratio is  $150 \pm 28$  ppm. The uncertainty in the retrieved H<sub>2</sub>O mixing ratio is about 19% in total (Sindoni et al., 2011).

obtained by Subaru/IRCS data and H<sub>2</sub>O abundances retrieved from MEX/PFS data in order to investigate seasonal variation. HDO could not be detected from IRCS data with enough accuracy below 40°N owing to the high terrestrial humidity during the ground-based observation. Fig. 8 shows the latitudinal distribution of the H<sub>2</sub>O column density retrieved from PFS/SWC data (left panel) and the HDO column density retrieved from Subaru/IRCS data (right panel). These values have been normalized by surface pressure to remove the effect of topography. We found that both H<sub>2</sub>O and HDO column

densities have a large value in the polar region during the northern summer ( $L_s = 96^\circ$ ).

In order to derive the HDO/H<sub>2</sub>O ratio from these data, we calculated the mean profile of H<sub>2</sub>O column density retrieved from PFS with the latitudinal grid of the SUBARU observation. For that, the H<sub>2</sub>O column densities within the latitudinal footprint of SUBARU observation (i.e., atmospheric seeing during the observation) were averaged. The red curve in the left panel of Fig. 8 shows the mean profile of H<sub>2</sub>O column density. The black points shown in Fig. 9 represent the HDO/H<sub>2</sub>O ratio calculated by the profiles, and the red curve shown in Fig. 9 is the averaged HDO/H<sub>2</sub>O ratio in order to compare with that of  $L_s = 52^\circ$  (the blue curve shown in Fig. 9). The mean value (averaged over all observed longitudes and latitudes) of the HDO/H<sub>2</sub>O ratio at  $L_s = 96^\circ$  and its standard deviation are  $4.4 \pm 1.0$  wrt VSMOW. Although the error values are relatively large (mainly owing to the standard deviation of the H<sub>2</sub>O column density from PFS data and longitudinal variability), the latitudinal distribution of HDO/H<sub>2</sub>O ratio at  $L_s = 96^\circ$  is more uniform profile than the one observed at  $L_s = 52^\circ$ . An interesting result from Fig. 9 is the seasonal variation of HDO/H<sub>2</sub>O ratio over the latitude range between 70°N and 80°N. We found that the HDO/H<sub>2</sub>O ratio increased from  $2.4 \pm 0.6$  wrt VSMOW ( $L_s = 52^\circ$ ) to  $5.5 \pm 1.1$  wrt VSMOW ( $L_s = 96^\circ$ ) at the high latitude. As described in Section 4, the relatively low value of the HDO/H<sub>2</sub>O ratio at  $L_s = 52^\circ$  can be explained by condensation of water vapor. Since the water vapor abundances in the polar region exhibit a drastic increase from  $L_s = 52^\circ$  to  $L_s = 96^\circ$ , the seasonal increase of the HDO/H<sub>2</sub>O ratio from  $L_s = 52^\circ$  to  $L_s = 96^\circ$  can be considered to be due to sublimation of the polar water ice cap. Moreover, this relatively uniform latitudinal distribution of HDO/H<sub>2</sub>O ratio  $L_s = 96^\circ$  implies that the isotopic fractionation during sublimation is small and is beyond the sensitivity of this analysis. The observed seasonal variation suggests that the sublimation–condensation process can induce a change in the isotopic fractionation by a factor of 2.

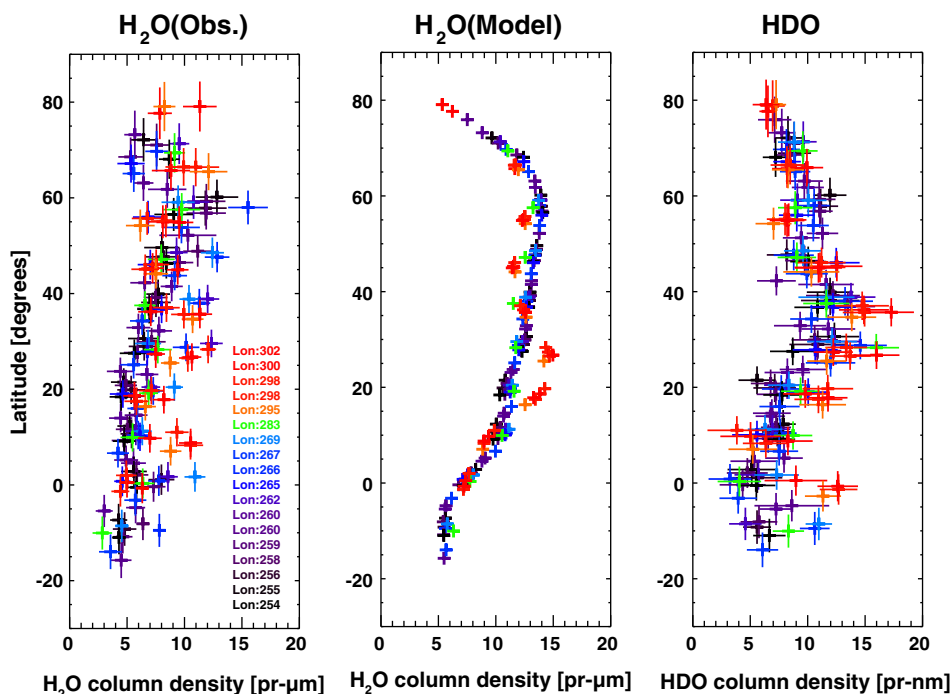


**Fig. 6.** (Left) Latitudinal distribution of H<sub>2</sub>O abundances measured by Subaru/IRCS. (Middle) Latitudinal distribution of H<sub>2</sub>O abundances predicted by the Mars Climate Database (ver5.0). (Right) Latitudinal distribution of HDO abundances measured by Subaru/IRCS. Differences in colors show the observing longitudes. The values are divided by ( $P_{surf}/6.1$ ) to remove the effect of topography, where  $P_{surf}$  is surface pressure in mbar. The horizontal bars show the estimated error values and the vertical bars represent the latitudinal footprints of the binned 10 pixels. (For interpretation of the references to color in this figure legend, the reader is referred to the web version of this article.)

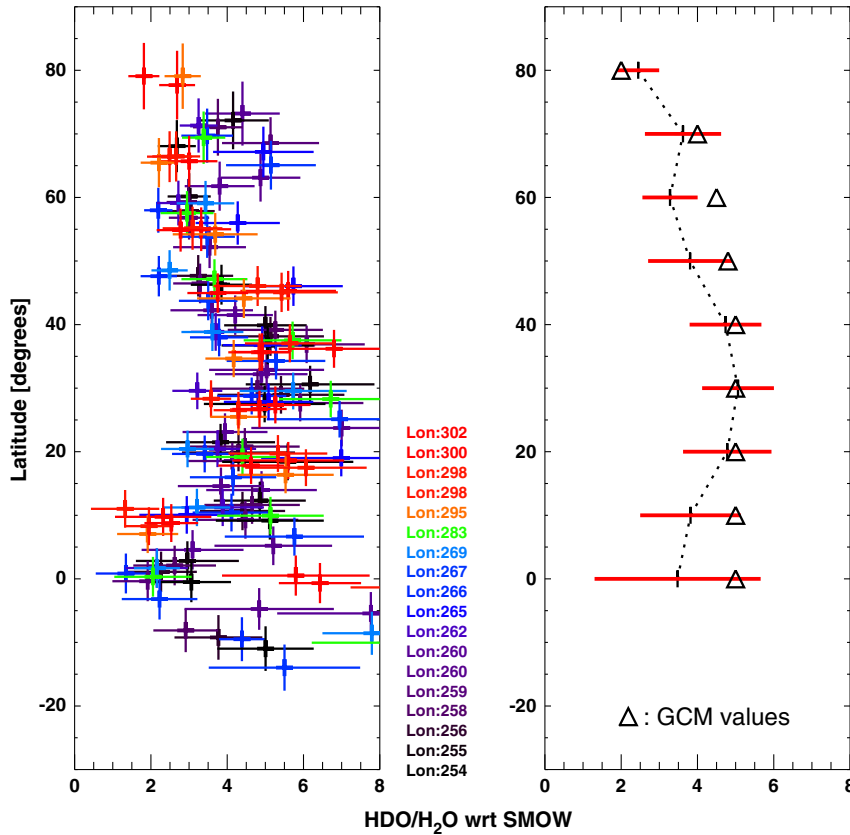


**Fig. 7.** (Left) Latitudinal distribution of the HDO/H<sub>2</sub>O ratio (relative value to VSMOW) measured by Subaru/IRCS. Differences in color represent the observed longitudes. The horizontal bars show the estimated error values and the vertical bars represent the latitudinal footprints of the binned 10 pixels. (Right) Latitudinal mean values of the HDO/H<sub>2</sub>O ratios are shown in the top panel. The error bars correspond to standard deviations. The triangle symbols show the predicted values by GCM of Montmessin et al. (2005). The values are extracted from the zonal averaged map of the HDO/H<sub>2</sub>O ratio shown in Fig. 2 of Montmessin et al. (2005). (For interpretation of the references to color in this figure legend, the reader is referred to the web version of this article.)

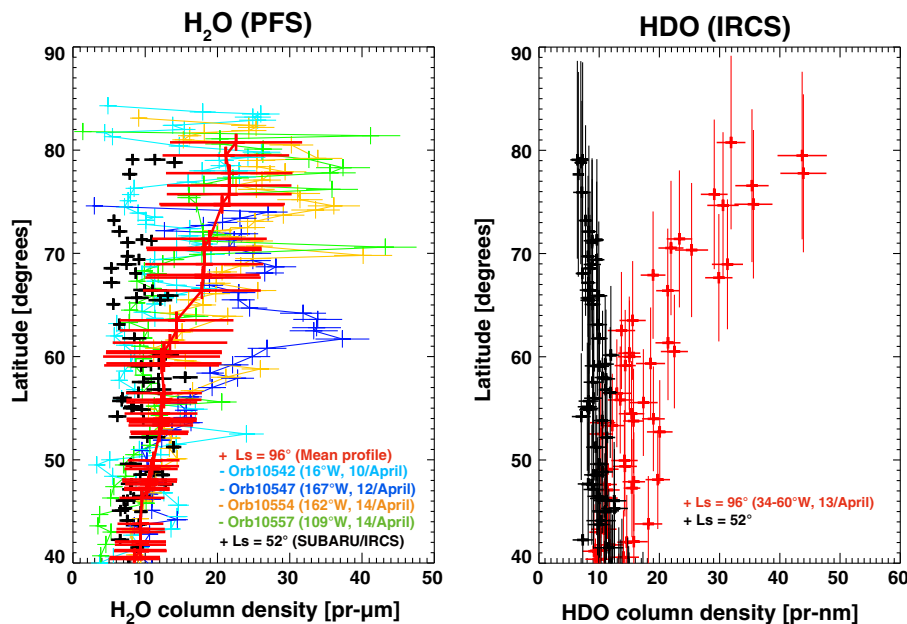


**Fig. 8.** (Left) Latitudinal distribution of the H<sub>2</sub>O column density retrieved from MEX/PFS-SWC observations. The light blue, blue, yellow, and green curves represent orbit10542 (16°W, 10/April), orbit10547 (167°W, 12/April), orbit10554 (162°W, 14/April), and orbit10557 (109°W, 14/April), respectively. The red curve corresponds to the longitudinal mean profile and the error bars represent standard deviation. The black points show the H<sub>2</sub>O column density at Ls = 52° (northern spring) retrieved by Subaru/IRCS. (Right) Latitudinal distribution of the HDO column density retrieved from Subaru/IRCS observations. The red and black points represent the values at Ls = 96° (northern summer) and Ls = 52° (northern spring), respectively. The blue curve denotes the longitudinal mean profile of the retrieved HDO column density at Ls = 96° and the error bars represent standard deviation. These values have been normalized by surface pressure in order to remove the effect of topography. (For interpretation of the references to color in this figure legend, the reader is referred to the web version of this article.)

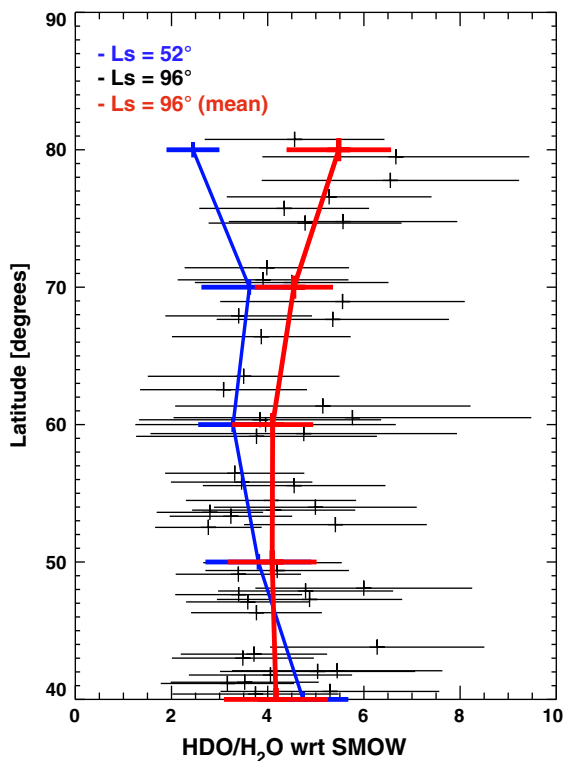


**Fig. 9.** Seasonal variation of the HDO/H<sub>2</sub>O ratio (relative to VSMOW). The red curve represents the distribution observed at  $L_s = 96^\circ$  and the black curve indicates the distribution at  $L_s = 52^\circ$  (similar to the right panel of Fig. 7). The error values of the HDO/H<sub>2</sub>O ratio at  $L_s = 96^\circ$  are estimated from standard deviations of both H<sub>2</sub>O and HDO mixing ratios. (For interpretation of the references to color in this figure legend, the reader is referred to the web version of this article.)

Note that the IRCS and PFS measurements were taken at different local times on Mars (IRCS: 9–10 h, PFS: 16 h). This may cause systematic error in the retrieved HDO/H<sub>2</sub>O ratio. However, Phoenix measurements showed no significant difference in H<sub>2</sub>O abundance between 9 h and 16 h (Smith et al., 2009b). Moreover, recent remote-sensing studies by MEX/SPICAM and MGS/TES show that local time variation of total H<sub>2</sub>O column is small at this season (e.g., Pankine and Tamppari, 2015; Trokhimovskiy et al., 2015). The systematic error in the HDO/H<sub>2</sub>O ratio can be estimated to be less than  $\sim 10\%$ . Therefore, we assume that the systematic error in the HDO/H<sub>2</sub>O ratio due to using the different local time observations by IRCS and PFS can be less than  $\sim 10\%$ . The seasonal increase of HDO/H<sub>2</sub>O ratio over the latitude range between  $70^\circ\text{N}$  and  $80^\circ\text{N}$  is still significant even if the systematic error is taken into account.

## 6. Geographical distribution over low latitudes at $L_s = 52^\circ$ (northern spring)

We investigated the geographical distribution of the HDO/H<sub>2</sub>O ratio over low latitudes at the northern spring ( $L_s = 52^\circ$ ) in the longitudinal range between  $220^\circ\text{W}$  and  $360^\circ\text{W}$ , including various local times from 10 h to 17 h. Fig. 10 shows the longitudinal distribution of column-integrated H<sub>2</sub>O and HDO abundances retrieved from the Subaru/IRCS observations carried out on January 4, 2012. These values have been normalized by surface pressure in order to remove the effect of topography. The retrieved H<sub>2</sub>O abundances are distributed in the range from 4 pr- $\mu\text{m}$  to 18 pr- $\mu\text{m}$ , and the

HDO abundances range from 5 pr-nm to 19 pr-nm. The retrieved H<sub>2</sub>O abundances are consistent with the typical abundance during this season reported by the space-borne observations. For example, MGS/TES and Viking/MAWD results determined that the longitudinal mean abundances at this season are between 10 pr- $\mu\text{m}$  and 15 pr- $\mu\text{m}$  (e.g., Smith, 2002). The retrieved longitudinal distribution of water vapor exhibits a local maximum over Arabia Terra ( $\sim 330^\circ\text{W}$ ), according to both H<sub>2</sub>O and HDO abundances. Fig. 11 illustrates the longitudinal distribution of the HDO/H<sub>2</sub>O ratio retrieved from the Subaru/IRCS observations (top panel) and the value averaged over all latitudes (bottom panel). The global mean value of the derived HDO/H<sub>2</sub>O ratio and its standard deviation are  $5.1 \pm 1.2$  wrt VSMOW. The local enhancement of water vapor abundances over Arabia Terra has been depicted in a seasonal-averaged map of water vapor using spacecraft-borne measurements with MGS/TES (Smith, 2002) and MEX/PFS (Fouchet et al., 2007; Tschimmel et al., 2008; Sindoni et al., 2011). On the other hand, as shown in Fig. 11, there is no significant longitudinal variation in the HDO/H<sub>2</sub>O ratio. Although the results cannot constrain the sources of local enhancement, i.e., atmospheric dynamics or sublimation from subsurface ice, we have demonstrated that there is no significant longitudinal distribution over Arabia Terra.

These observations also covered different local times ranging from 10 h to 17 h, although not for the same longitudes. Fig. 12 shows the local time distribution of H<sub>2</sub>O and HDO abundances normalized by surface pressure. The retrieved water vapor exhibits a local maximum around 12–13 h that corresponds to Arabia Terra ( $\sim 330^\circ\text{W}$ ). Fig. 13 represents the local time dependence of the HDO/H<sub>2</sub>O ratio retrieved from the Subaru/IRCS observation. It shows that the distribution of HDO/H<sub>2</sub>O is no significant variation ( $5.1 \pm 1.2$  with respect to VSMOW) in the local time range between 10 h and 17 h. Note that recent observations reveal a significant depletion of HDO at dawn that may be explained by condensation-induced fractionation due to cloud formation (Villanueva et al., 2008, 2013; Novak et al., 2014). Further observation is needed to address this issue because the dawn side was not covered by our observations.

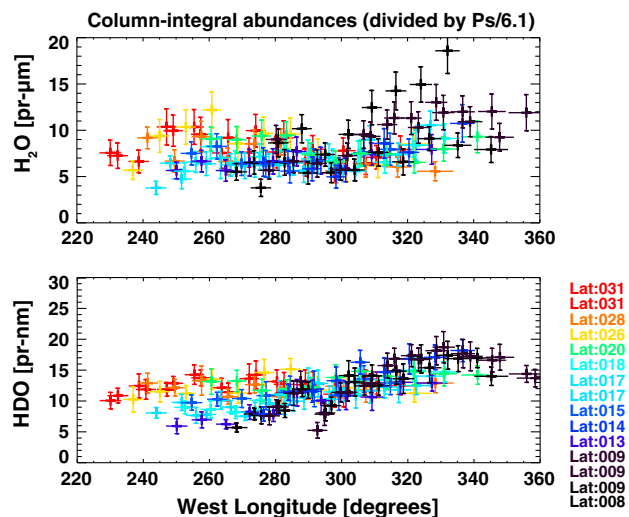


**Fig. 10.** (Top) Longitudinal distribution of H<sub>2</sub>O column abundances. (Bottom) Longitudinal distribution of HDO column abundances. Differences in colors represent the observing latitudes. The values are divided by ( $P_{surf}/6.1$ ) to remove the effect of topography, where  $P_{surf}$  is surface pressure in mbar. The vertical bars denote the estimated error values and the horizontal bars represent the longitudinal footprints of the binned 10 pixels. (For interpretation of the references to color in this figure legend, the reader is referred to the web version of this article.)

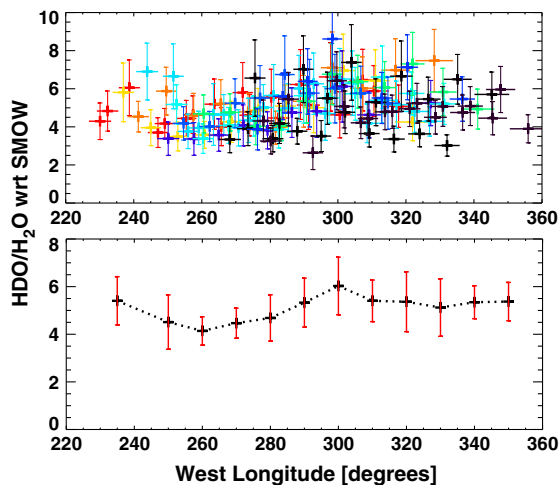


**Fig. 11.** (Top) Longitudinal distribution of the HDO/H<sub>2</sub>O ratio (relative value to VSMOW; HDO/H<sub>2</sub>O =  $3.11 \times 10^{-4}$ ). Differences in colors signify the observing latitudes. The vertical bars show the estimated error values and the horizontal bars represent the longitudinal footprints of the binned 10 pixels. (Bottom) Latitudinal-mean values of the HDO/H<sub>2</sub>O ratios shown in the top panel. The error bars correspond to their standard deviations. (For interpretation of the references to color in this figure legend, the reader is referred to the web version of this article.)

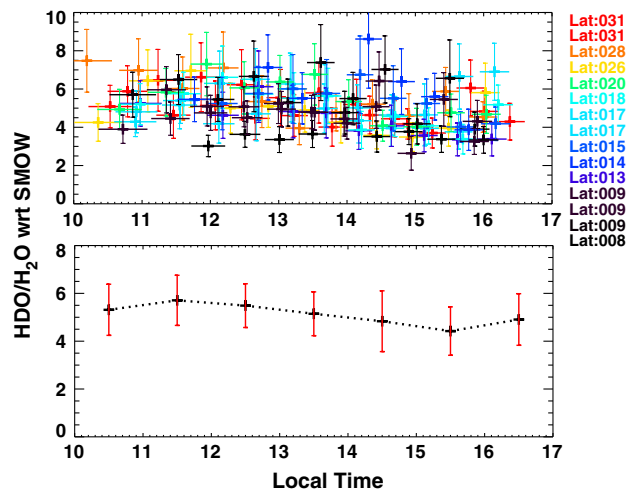


**Fig. 13.** (Top) Local time distribution of the HDO/H<sub>2</sub>O ratio. Differences in colors denote the observing latitudes. (Bottom) Latitudinal-mean values of the HDO/H<sub>2</sub>O ratios shown in the top panel. The error bars correspond to their standard deviations. (For interpretation of the references to color in this figure legend, the reader is referred to the web version of this article.)

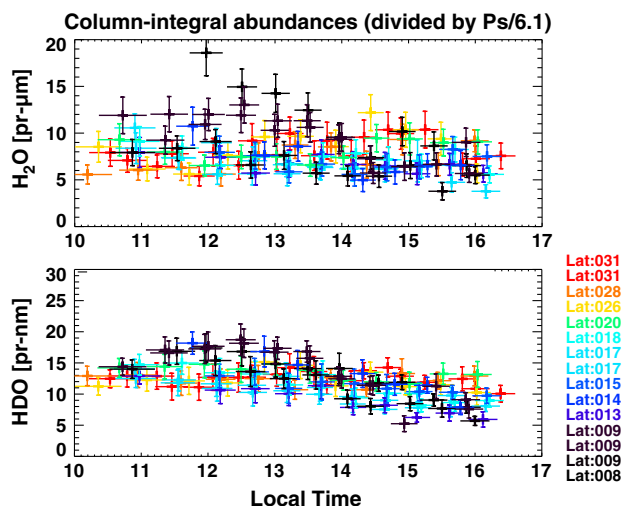


**Fig. 12.** (Top) Local time distribution of H<sub>2</sub>O column abundances. (Bottom) Local time distribution of HDO column abundances. Differences in colors represent the observing latitudes. (For interpretation of the references to color in this figure legend, the reader is referred to the web version of this article.)

## 7. Comparison with the previous observations

The latitudinal mean HDO/H<sub>2</sub>O ratios retrieved from our observations are  $4.1 \pm 1.4$  ( $L_s = 52^\circ$ ) and  $4.4 \pm 1.0$  ( $L_s = 96^\circ$ ) wrt VSMOW, which agrees with the global mean values reported with previous ground-based observations by Owen et al. (1988) [ $6 \pm 3$  wrt VSMOW] and Krasnopolsky et al. (1997) [ $5.5 \pm 2.0$  wrt VSMOW] but smaller than the value reported by Villanueva et al. (2015) [ $\sim 7$  wrt VSMOW]. One possible explanation for this discrepancy is temporal variation of the HDO/H<sub>2</sub>O ratio (seasonal, localtime, or inter-annual variation). The other possible explanation is due to systematic error in the analysis. For instance, in this analysis, the effect of dust and water ice was not taken into account. This may give an impact the retrieved HDO abundance (see SOM of Villanueva et al., 2015). The implementation of the aerosol effect in our retrieval is one of the future works.

As shown in Fig. 7, we found that the retrieved latitudinal distribution at  $L_s = 52^\circ$  exhibits a maximum around sub-solar latitudes ( $20\text{--}40^\circ\text{N}$ ) and decreases at high latitudes ( $>60^\circ\text{N}$ ), which was also found by Novak et al. (2011). The observation by Novak et al. (2011) was performed in the same season ( $L_s = 50^\circ$ ) as our observation but for a different martian year (MY 29), longitude ( $153^\circ\text{W}$ ), and local time (9:40) by the IRTF/CSHELL. The HDO/H<sub>2</sub>O ratio retrieved by Novak et al. (2011) peaks at  $6.9 \pm 0.2$  wrt VSMOW in the sub-solar region and decreases to  $3.8 \pm 0.3$  toward the pole. Although our values are smaller than those obtained by Novak et al. (2011), the two observations have a similar distribution that peaks near the sub-solar latitude and decreases toward the pole. Moreover, Villanueva et al. (2015) reported the map of HDO/H<sub>2</sub>O ratio taken by the IRTF/CSHELL in the same season ( $L_s = 50^\circ$ ), the same martian year (MY 29), and including same longitude ( $153^\circ\text{W}$ ) of the observation by Novak et al. (2011). However, the map by Villanueva et al. (2015) does not show the depletion of HDO at the high latitudes region. Villanueva et al. (2015) also revealed correlation between HDO/H<sub>2</sub>O ratio and H<sub>2</sub>O column abundance. The positive correlation is agreed with the concept of the Rayleigh distillation considered in the GCM model (Montmessin et al., 2005). On the other hand, Fisher et al. (2008) reported that the HDO/H<sub>2</sub>O ratio is very large when the atmosphere's water vapor column is small from the data by Mumma et al. (2003). The anti-correlation between H<sub>2</sub>O column density and HDO/H<sub>2</sub>O ratio was interpreted as the possible effect of existence of multiple ice reservoirs having different HDO/H<sub>2</sub>O ratios depending on their size, accessibility, and location. Fig. 14 shows the relationship between H<sub>2</sub>O column density and HDO/H<sub>2</sub>O ratio from our results. Our result at  $L_s = 52^\circ$  also suggests the anti-correlation. Further observations are necessary to constrain these issues. Furthermore, Villanueva et al. (2015) reported possible anti-correlation between HDO/H<sub>2</sub>O ratio and surface altitude. Although possible regionalism could be seen in our results, we cannot make sure if it is real variation since the error values are large. Regionalism of HDO/H<sub>2</sub>O is beyond the scope of this paper.

As shown in Fig. 11, we found that the HDO/H<sub>2</sub>O ratio was no significant variation ( $5.1 \pm 1.2$  wrt VSMOW) in the longitudinal range between  $220^\circ\text{W}$  and  $360^\circ\text{W}$  at  $L_s = 52.4^\circ$ . Novak et al. (2014, conference proceeding) reported the longitudinal distribution of HDO/H<sub>2</sub>O ratio over the same area but at different season ( $L_s = 72.5^\circ$ ). The HDO/H<sub>2</sub>O ratio at  $L_s = 72.5^\circ$  reported by Novak

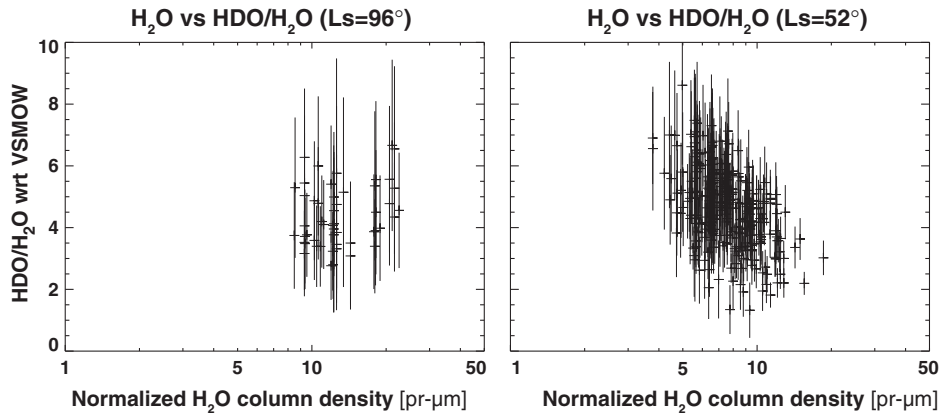


Fig. 14. HDO/H<sub>2</sub>O ratio with H<sub>2</sub>O column density from our measurements at L<sub>s</sub> = 96° (left) and L<sub>s</sub> = 52° (right).

et al. (2014) is distributed between 2 and 5 wrt VSMOW (see the Fig. 3B of Novak et al. (2014)). The HDO/H<sub>2</sub>O values are lower than those of our results at L<sub>s</sub> = 52.4°. Although the reason is not clear at the moment, the seasonal variation of HDO/H<sub>2</sub>O ratio at low latitudes could be related with the fact that Villanueva et al. (2015) found very low HDO/H<sub>2</sub>O ratio (1–3 wrt VSMOW) at the winter hemisphere. Similar seasonal decrease of the HDO/H<sub>2</sub>O ratio at

the low-latitude region also can be seen in the maps (at L<sub>s</sub> = 50° and 80°) reported by Villanueva et al. (2015).

8. Summary

In this study, seasonal variation of HDO/H<sub>2</sub>O distributions by latitude during the northern spring (L<sub>s</sub> = 52°) and summer (L<sub>s</sub> = 96°)

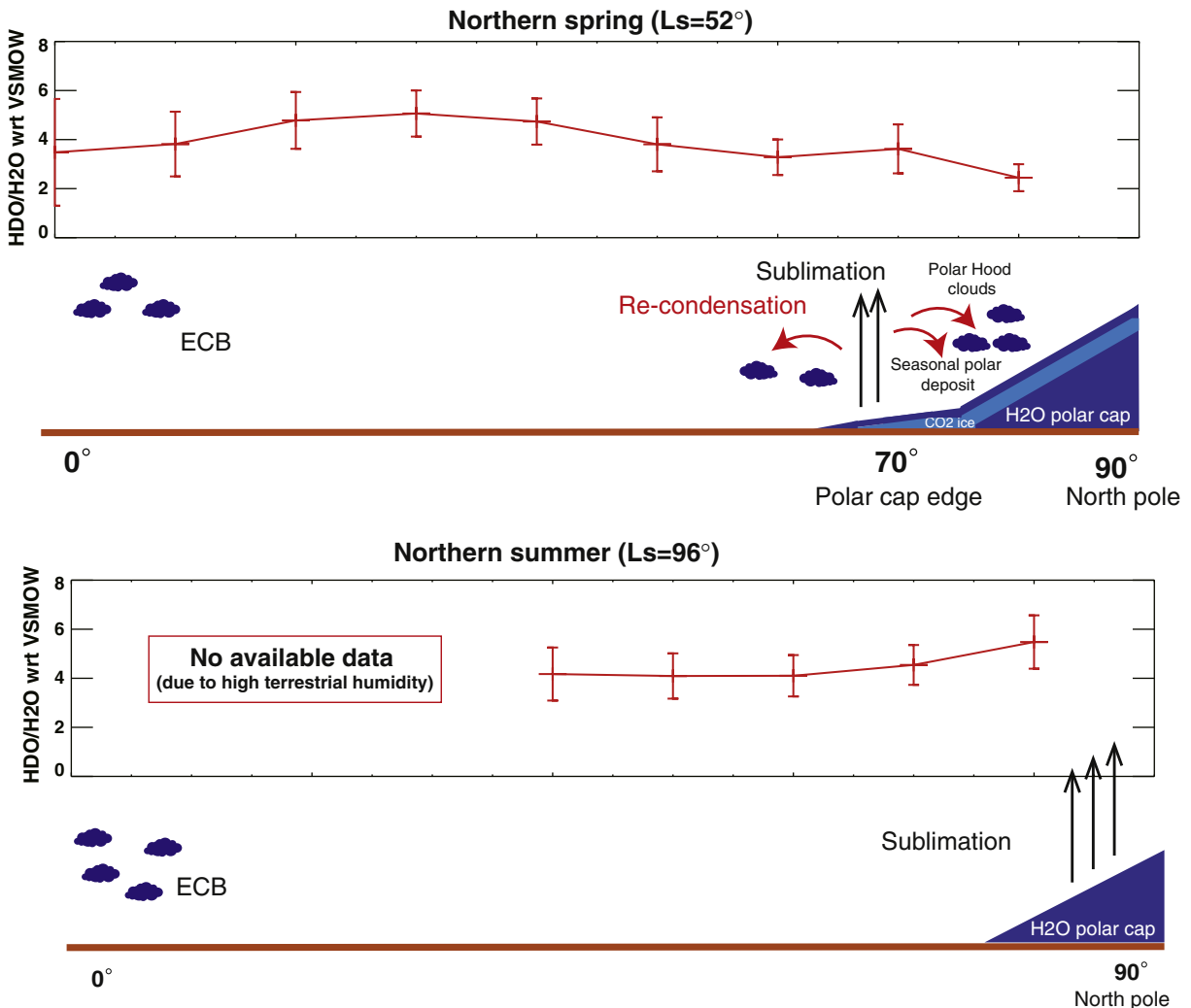


Fig. 15. Sublimation–condensation process in the martian water cycle and the HDO/H<sub>2</sub>O ratio in water vapor during the northern spring (L<sub>s</sub> = 52°) and summer (L<sub>s</sub> = 96°), inferred from our observations.

was investigated. The derived seasonal variation of the HDO/H<sub>2</sub>O ratio and global view of the water cycle on Mars inferred from our observations is summarized in Fig. 15. We found seasonal increase of the HDO/H<sub>2</sub>O ratio at the polar region (70–80°N), from  $2.4 \pm 0.6$  wrt VSMOW ( $L_s = 52^\circ$ ) to  $5.1 \pm 0.7$  wrt VSMOW ( $L_s = 96^\circ$ ). The seasonal increase can be explained by the interaction between the atmosphere and the north polar cap: condensation of water vapor occurs as polar hood clouds and/or the seasonal polar cap form in the northern spring ( $L_s = 52^\circ$ ), and sublimation of the polar water ice cap occurs in the northern summer ( $L_s = 96^\circ$ ). On the other hand, the latitudinal mean HDO/H<sub>2</sub>O ratios do not show a significant seasonal variation, with values of  $4.1 \pm 1.4$  ( $L_s = 52^\circ$ ) and  $4.6 \pm 0.7$  ( $L_s = 96^\circ$ ). We found the HDO/H<sub>2</sub>O ratio has no significant variation ( $5.1 \pm 1.2$  wrt VSMOW) over low latitudes during the northern spring in the longitudinal range between 220°W and 360°W for different local times from 10 h to 17 h. As shown in Fig. 15, we did not take into account the effects of subsurface–atmosphere interaction in the interpretation of the results since it is still unknown that how much the ground ice interacts with atmospheric water vapor and how much they induce isotopic fractionations. However, our results suggest that HDO/H<sub>2</sub>O distribution in the atmosphere is mainly controlled by condensation-induced fractionation between the northern polar cap and the atmosphere.

Still, further observations are necessary to conduct open issues. For example, relationship between H<sub>2</sub>O column density and HDO/H<sub>2</sub>O ratio and its interpretation are not fully understood. Very low HDO/H<sub>2</sub>O ratio (1–3 wrt VSMOW) at the winter hemisphere reported by Villanueva et al. (2015) might be related to subsurface–atmosphere interaction. In order to increase data set, we plan to investigate the HDO/H<sub>2</sub>O ratio by comparing between the HDO map observed by IRTF/TEXES (e.g., Encrenaz et al., 2010) and the H<sub>2</sub>O map retrieved from MEX/PFS. In addition, Nadir and Occultation for Mars Discovery (NOMAD) onboard ExoMars Trace Gas Orbiter (Vandaele et al., 2011) will perform to measure maps of HDO/H<sub>2</sub>O ratio and its vertical profile are obtained from the Mars Orbiter. It will allow us to obtain a complete picture of its geographical and seasonal distributions.

## Acknowledgments

This work was supported by a grant-in-aid for JSPS Fellows (#233113). This work was also supported by a grant-in-aid for Scientific Research (22340142, 24403007, and 15H05209) from the Japan Society for the Promotion of Science, the Tohoku University Global COE program titled “Global Education and

Research Center for Earth and Planetary Dynamics.”, and European Union FP7 CrossDrive Project. The presented analysis is based on data collected at the Subaru telescope, which is operated by the National Astronomical Observatory of Japan (NAOJ). We express our thanks to Dr. T.S. Pyo and Dr. Y. Minowa for their kind advice and helpful support for the operation of IRCS. ASI funds PFS activities in the context of Italian participation in the ESA Mars Express mission. E. Millour and F. Forget provided the Mars Climate Database. We thank Dr. Kei Yoshimura for his useful suggestions on HDO/H<sub>2</sub>O isotopic fractionation during the sublimation–condensation process.

## Appendix A. Retrieval of instrumental line shape of IRCS

Since line widths of the martian H<sub>2</sub>O and HDO lines are  $\sim 10$  times smaller than the spectral resolution of IRCS, the observed line shapes reflect the instrumental line shape (ILS) of IRCS. Therefore, characterization of the ILS is important to perform retrieval accurately. Here, we retrieved the ILS using Ar lamp measurements carried out in a similar configuration to the Mars observation. The lamp measurements were performed for 2.5 h in order to obtain sufficient signal to noise ratio. Line widths of Ar lamps are so narrow ( $\sim 0.02$  cm<sup>-1</sup>, Engleman et al., 2003) that the observed line shapes represent the ILS of IRCS. There are five independent lines in the measured spectral ranges (3016.7336 cm<sup>-1</sup>, 3023.0817 cm<sup>-1</sup>, 3040.5647 cm<sup>-1</sup>, 3191.5201 cm<sup>-1</sup>, and 3272.9622 cm<sup>-1</sup>), and we used lines at 3040.5647 cm<sup>-1</sup>, 3191.5201 cm<sup>-1</sup>, and 3272.9622 cm<sup>-1</sup> for retrieval of the ILS. Fig. A1 shows all the measurements for the three lines. We found that full width at half maximum (FWHM) of the ILS is not constant but depends on pixel position on the detector.

We attempted to retrieve the ILS as a function of FWHM. As the first attempt, Gaussian and sinc-squared functions were applied to fit these data since these functions are well known as a line shape of echelle spectroscopy. However, as shown in Fig. A2, both functions could not reproduce the observed line shape, especially in the wings. Therefore, we assumed that the ILS is a combination of two functions, one for line center and the other for wings. We tested the six cases listed in Table A1 and determined the most accurate one by using the least squares method. We derived the switching spectral point of the two functions and the relationship between their FWHMs in the retrieval process.

As shown in Table A1, the combination of two Gaussian functions is most accurate for the ILS of IRCS. The retrieved ILS of IRCS is given by

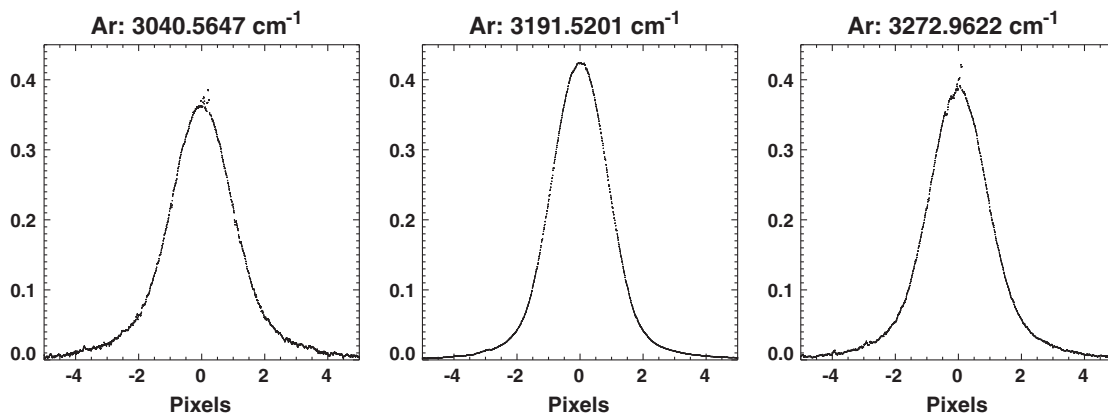
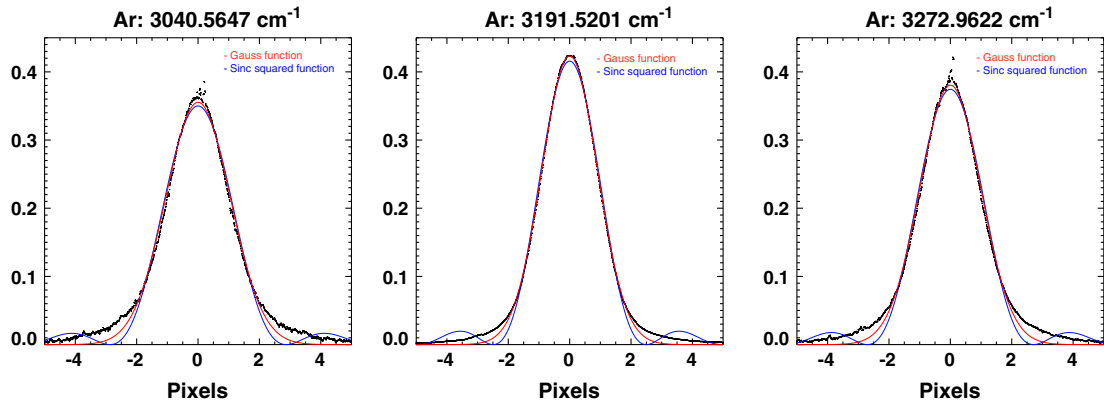
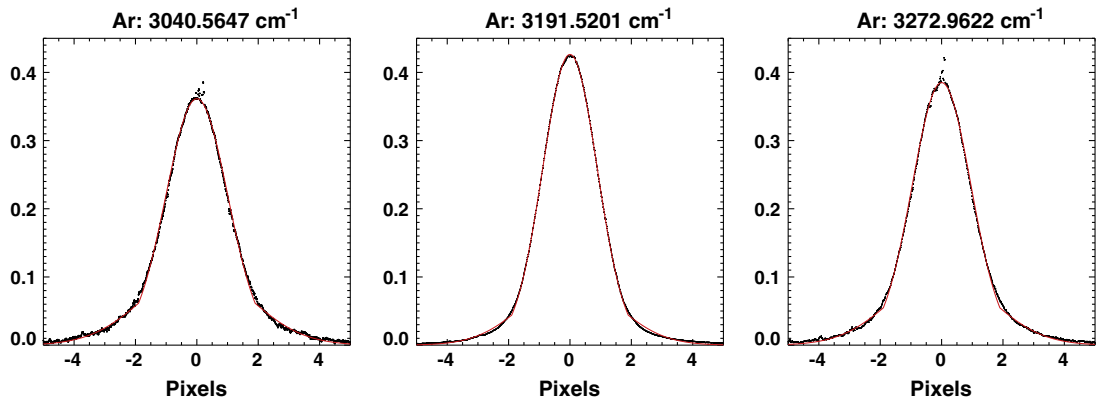


Fig. A1. Ar lamp spectra measured by IRCS at 3049.5647 cm<sup>-1</sup> (left), 3191.5201 cm<sup>-1</sup> (center), and 3272.9622 cm<sup>-1</sup> (right). All observed data (all pixels in the slit) are shown together.



**Fig. A2.** Ar lamp spectra shown in Fig. A1 and their best-fit spectra with Gaussian function (red curves) and sinc-squared function (blue curves). (For interpretation of the references to color in this figure legend, the reader is referred to the web version of this article.)



**Fig. A3.** Ar lamp spectra shown in Fig. A1 and the retrieved ILS by combination of two Gaussian functions (red curves). (For interpretation of the references to color in this figure legend, the reader is referred to the web version of this article.)

$$ILS(x) = \begin{cases} F_1(x) & (|x - x_0| \leq 1.9 \text{ pixels}) \\ F_2(x) & (|x - x_0| > 1.9 \text{ pixels}) \end{cases},$$

where

$$F_1(x) = \exp\left(-\frac{(x-x_0)^2}{w_{ILS}^2}\right),$$

$$F_2(x) = \beta \times \exp\left(-\frac{(x-x_0)^2}{w'_{ILS}{}^2}\right), \quad w'_{ILS} = w_{ILS} \times 1.72,$$

$$\beta = F_1(1.9) / \exp(-(1.9/w_{ILS})^2/2).$$

$w_{ILS}$  and  $w'_{ILS}$  are FWHM of the Gaussian functions. The FWHM of the second function (for line wing) is 1.72 times larger than that of the first function (for line center). The two functions are switched at the 1.9 pixel far from the observed wavelength. Fig. A3 shows the Ar lamp measurements and the retrieved ILS. The IRCS could reproduce the wings of the lamp spectra much better than simple Gaussian or sinc-squared function (Fig. A2).

**Table A1**

List of combinations tested in retrieval of the ILS.

	1st function (for line center)	2nd function (for line wing)	Chi-square (relative values)
Case-1	Gauss	Gauss	1.00
Case-2	Lorenz	Lorenz	5.19
Case-3	Gauss	Lorenz	1.38
Case-4	Lorenz	Gauss	5.17
Case-5	Sinc	Gauss	2.31
Case-6	Sinc	Lorenz	2.43

## References

- Appéré, T. et al., 2011. Winter and spring evolution of northern seasonal deposits on Mars from OMEGA on Mars Express. *J. Geophys. Res.* 116, E05001.
- Benson, J.L., Kass, D.M., Kleinböhl, A., 2011. Mar's north polar hood as observed by the Mars Climate Sounder. *J. Geophys. Res.* 116, E03008.
- Boyton, W.V. et al., 2002. Distribution of hydrogen in the near surface of Mars: Evidence for subsurface ice deposits. *Science* 297, 81–85.
- Christensen, P.R. et al., 2001. The Mars Global Surveyor Thermal Emission Spectrometer experiment: Investigation description and surface science results. *J. Geophys. Res.* 106, 23823–23871.
- Encrenaz, T. et al., 2010. Water vapor map of Mars near summer solstice using ground-based infrared spectroscopy. *Astron. Astrophys.* 520, A33.
- Engleman Jr., R., Hinkle, K.H., Wallace, L., 2003. The near-infrared spectrum of a Th/Ar hollow cathode lamp. *J. Quant. Spectrosc. Radiat. Trans.* 78, 1–30.
- Farmer, C.B. et al., 1977. Mars: Water vapor observations from the Viking orbiters. *J. Geophys. Res.* 82, 4225–4248.
- Fedorova, A. et al., 2006. Mars water vapor abundance from SPICAM IR spectrometer: Seasonal and geographic distributions. *J. Geophys. Res.* 111, E09S08.
- Feldman, W.C. et al., 2004. Global distribution of near-surface hydrogen on Mars. *J. Geophys. Res.* 109, E09006.
- Fisher, D.A., 2007. Mars' water isotope (D/H) history in the strata of the Northern polar cap: Inferences about the water cycle. *Icarus* 187, 430–441.
- Fisher, D.A., Novak, R., Mumma, M.J., 2008. D/H ratio during the northern polar summer and what the Phoenix mission might measure. *J. Geophys. Res.* 113, E00A15.
- Formisano, V. et al., 2005. The Planetary Fourier Spectrometer (PFS) onboard the European Mars Express mission. *Planet. Space Sci.* 53 (10), 963–974.
- Fouchet, T., Lellouch, E., 2000. Vapor pressure isotope fractionation effects in planetary atmospheres: Application to deuterium. *Icarus* 144, 114–123.
- Fouchet, T. et al., 2007. Martian water vapor: Mars Express PFS/LW observations. *Icarus* 190, 32–49.
- Frankenberg, C. et al., 2009. Dynamic processes governing lower-tropospheric HDO/H<sub>2</sub>O ratios as observed from space and ground. *Science* 325, 1374–1377.
- Gamache, R. et al., 2000. Total internal partition sums for molecules in terrestrial atmosphere. *J. Mol. Struct.* 517–518, 407–425.

- Hase, F. et al., 2010. The ACE–FTS atlas of the infrared solar spectrum. *J. Quant. Spectrosc. Radiat. Trans.* 111, 521–528.
- Ignatiev, N.I., Grassi, D., Zasova, L.V., 2005. Planetary Fourier spectrometer data analysis: Fast radiative transfer models. *Planet. Space Sci.* 53, 1035–1042.
- Kobayashi, N. et al., 2000. IRCS: Infrared camera and spectrograph for the Subaru telescope. In: Iye, M., Moorwood, A.F. (Eds.), *Proceedings of the SPIE 4008: Optical and IR Telescope Instrumentation and Detectors*, p. 1056.
- Krasnopolsky, V.A. et al., 1997. High-resolution spectroscopy of Mars at 3.7 and 8  $\mu\text{m}$ : A sensitive search of  $\text{H}_2\text{O}_2$ ,  $\text{H}_2\text{CO}$ ,  $\text{HCl}$ , and  $\text{CH}_4$ , and detection of  $\text{HDO}$ . *J. Geophys. Res.* 102 (E3), 6525–6534.
- Krasnopolsky, V.A., Maillard, J.P., Owen, T.C., 2004. Detection of methane in the martian atmosphere: Evidence for life? *Icarus* 172, 537–547.
- Maltagliati, L. et al., 2008. Observations of atmospheric water vapor above the Tharsis volcanoes on Mars with the OMEGA/MEX imaging spectrometer. *Icarus* 194, 53–64.
- Montmessin, F. et al., 2004. Origin and role of water ice clouds in the martian water cycle as inferred from a general circulation model. *J. Geophys. Res.* 109, E10004.
- Montmessin, F., Fouchet, T., Forget, F., 2005. Modeling the annual cycle of  $\text{HDO}$  in the martian atmosphere. *J. Geophys. Res.* 110, E03006.
- Moore, J.E. et al., 2012. Experimental and theoretical simulation of sublimating dusty water ice with implications for D/H ratios of water ice on Comets and Mars. *Planet. Sci.* 1, 1–30.
- Mumma, M.J. et al., 2003. Seasonal mapping of  $\text{HDO}$  and  $\text{H}_2\text{O}$ . In: *Sixth International Conference on Mars Atmosphere*, Abstract 3186, Jet Propulsion Lab., Pasadena, Calif.
- Novak, R.E., Mumma, M.J., Villanueva, G.L., 2011. Measurement of the isotopic signatures of water on Mars; implications for studying methane. *Planet. Space Sci.* 59, 163–168.
- Novak, R.E., Mumma, M.J., Villanueva, G.L., 2014. Diurnal mapping of  $[\text{H}_2\text{O}]$ ,  $[\text{HDO}]$ ,  $[\text{HDO}]/[\text{H}_2\text{O}]$ , and  $\text{O}_2(\text{a}^1\Delta_g)$  emission on Mars using ground based high-resolution spectroscopy. In: *The 5th International Workshop on the Mars Atmosphere: Modeling and Observation*, id.3402.
- Owen, T. et al., 1988. Deuterium on Mars: The abundance of  $\text{HDO}$  and the value of D/H. *Science* 240, 1767–1770.
- Pankine, A.A., Tamppari, L.K., 2015. Constrains on water vapor vertical distribution at the Phoenix landing site during summer from MGS TES day and night observations. *Icarus* 252, 107–120.
- Pankine, A.A., Tamppari, L.K., Smith, M.D., 2010. MGS TES observations of the water vapor above the seasonal and perennial ice caps during northern spring and summer. *Icarus* 210, 58–71.
- Rothman, L.S. et al., 1998. The HITRAN molecular spectroscopic database and HAWKS (HITRAN Atmospheric Workstation): 1996 edition. *J. Quant. Spectrosc. Radiat. Trans.* 60, 665–710.
- Rothman, L.S. et al., 2009. The HITRAN 2008 molecular spectroscopic database. *J. Quant. Spectrosc. Radiat. Trans.* 110, 533–572.
- Sindoni, G., Formisano, V., Geminale, A., 2011. Observations of water vapour and carbon monoxide in the martian atmosphere with the SWC of PFS/MEX. *Planet. Space Sci.* 59, 149–162.
- Smith, M.D., 2002. The annual cycle of water vapor on Mars as observed by the Thermal Emission Spectrometer. *J. Geophys. Res.* 107, E11.
- Smith, M.D., 2004. Interannual variability in TES atmospheric observations of Mars during 1999–2003. *Icarus* 167, 148–165.
- Smith, M.D. et al., 2009a. Compact Reconnaissance Imaging Spectrometer observations of water vapor and carbon monoxide. *J. Geophys. Res.* 114, E00D03.
- Smith, P.H. et al., 2009b.  $\text{H}_2\text{O}$  at the Phoenix landing site. *Science* 325, 58–61.
- Spinrad, H., Münch, G., Kaplan, L.D., 1963. Letter to the Editor: The detection of water vapor on Mars. *Astrophys. J.* 137, 1319–1321.
- Trokhimovskiy, A. et al., 2015. Mars' water vapor mapping by the SPICAM IR spectrometer: Five martian years of observations. *Icarus* 251, 50–64.
- Tschimmel, M. et al., 2008. Investigation of the water vapour on Mars with PFS/SW of Mars Express. *Icarus* 195, 557–575.
- Vandaele, A.C. et al., 2011. NOMAD, a spectrometer suite for nadir and solar occultation observations on the ExoMars Trace Gas Orbiter. *Proceedings of the Fourth International Workshop on the Mars Atmosphere: Modelling and Observation*, pp. 484–487.
- Villanueva, G.L. et al., 2008. Mapping the D/H of water on Mars using high-resolution spectroscopy. *Proceedings of the Third International Workshop on the Mars Atmosphere*, LPI Co 1447, p. 9101.
- Villanueva, G.L., Mumma, M.J., Novak, R.E., 2013. Hydrogen, oxygen, and carbon isotopic ratios in the martian atmosphere. *Proc. Lunar Sci. Conf., LPI Contribution No. 1719*, p. 2551.
- Villanueva, G.L. et al., 2015. Strong water isotopic anomalies in the martian atmosphere: Probing current and ancient reservoirs. *Science* 348, 218–221.
- Webster, C.R. et al., 2013. Isotope ratio of H, C, and O in  $\text{CO}_2$  and  $\text{H}_2\text{O}$  of the martian atmosphere. *Science* 341, 260–263.